

Rotate vector (Rv) reducer fault detection and diagnosis system: towards component level prognostics and health management (phm).



ROHAN, A., RAOUF, I. and KIM, H.S.

2020

© 2020 by the authors. Licensee MDPI, Basel, Switzerland.

Article

Rotate Vector (RV) Reducer Fault Detection and Diagnosis System: Towards Component Level Prognostics and Health Management (PHM)

Ali Rohan , Izaz Raouf and Heung Soo Kim * 

Department of Mechanical, Robotics and Energy Engineering, Dongguk University-Seoul, 30 Pil-dong 1 Gil, Jung-gu, Seoul 04620, Korea; Alirohan@dongguk.edu (A.R.); izazraouf@dongguk.edu (I.R.)

* Correspondence: heungsoo@dgu.edu; Tel.: +82-2-2260-8577

Received: 3 November 2020; Accepted: 27 November 2020; Published: 30 November 2020



Abstract: In prognostics and health management (PHM), the majority of fault detection and diagnosis is performed by adopting segregated methodology, where electrical faults are detected using motor current signature analysis (MCSA), while mechanical faults are detected using vibration, acoustic emission, or ferrography analysis. This leads to more complicated methods for overall fault detection and diagnosis. Additionally, the involvement of several types of data makes system management difficult, thus increasing computational cost in real-time. Aiming to resolve that, this work proposes the use of the embedded electrical current signals of the control unit (MCSA) as an approach to detect and diagnose mechanical faults. The proposed fault detection and diagnosis method use the discrete wavelet transform (DWT) to analyze the electric motor current signals in the time-frequency domain. The technique decomposes current signals into wavelets, and extracts distinguishing features to perform machine learning (ML) based classification. To achieve an acceptable level of classification accuracy for ML-based classifiers, this work extends to presenting a methodology to extract, select, and infuse several types of features from the decomposed wavelets of the original current signals, based on wavelet characteristics and statistical analysis. The mechanical faults under study are related to the rotate vector (RV) reducer mechanically coupled to electric motors of the industrial robot Hyundai Robot YS080 developed by Hyundai Robotics Co. The proposed approach was implemented in real-time and showed satisfying results in fault detection and diagnosis for the RV reducer, with a classification accuracy of 96.7%.

Keywords: prognostics and health management (PHM); fault detection and diagnosis; feature selection; machine learning

1. Introduction

With the advancement in the field of automation and control, modern industrial systems have adopted programmed robotics arrangements to execute tasks autonomously with minimum human interference. These robots act as basic building blocks in the automation of industrial systems, and over time, their continuous operation in manufacturing processes causes the degradation of constituent sub-systems and components. Without proper maintenance, this degradation can create several faults in the system, which in turn causes unexpected shutdowns and production loss to the manufacturers. To address this, researchers are creating novel health monitoring, diagnostics, prognostic, and maintenance strategies that are collectively known as prognostics and health management (PHM). PHM is a mechanism of preventive measures that deliver comprehensive and tailored solutions for the industrial health system, management, and prediction. In industrial systems, health refers to a certain industrial application or component's condition, efficiency, and remaining

useful lifetime (RUL). PHM can be seen as a systematic approach to effective and productive health management systems [1]. PHM combines the detection of an initiating fault (fault detection), isolation, recognition of its origin, fault type (fault diagnostics), and the prediction of the remaining useful life (prognostics). Figure 1 shows the basic architecture of the PHM system. PHM has become a critical method to identify system failures that can cause major damage to the environment and the user. It has emerged as an integral means of delivering a competitive advantage in the international market by enhancing efficiency, sustainability, security, and accessibility. In recent years, ideas and components of the PHM under different names have been developed independently in various fields that include mechanical, electrical engineering, and statistical science.

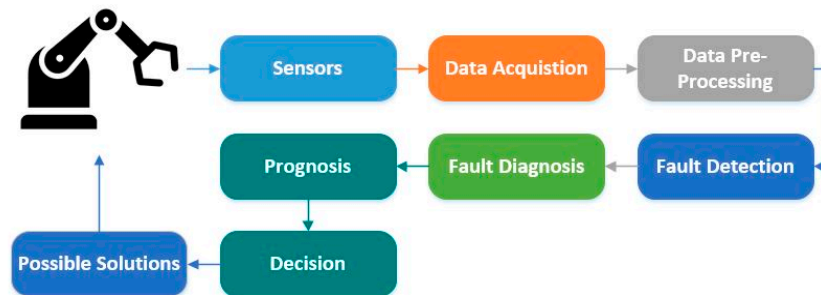


Figure 1. Basic architecture of a PHM system.

PHM can be utilized at both the component and system levels. Generally, the component level PHM focuses on monitoring the health of individual components (such as electrical and electronic devices, mechanical reducers, and engines), taking into account environmental, operational, and performance-related parameters to determine if the health of the monitored component is degraded by the time [2,3]. Meanwhile, the system level PHM analyzes the overall system health by taking into account the system architecture, system function, and process-related parameters [4]. Over the past years, there has been sustained research activity in PHM, especially with the immense development in the field of artificial intelligence (AI), to where it is now possible to create methodologies that utilize the decision-making capabilities of AI tools, such as deep learning (DL) and machine learning (ML), to develop a fault diagnostics and prognostics system in an efficacious way. Several researchers have been working on the design of such a system at both component and system levels. PHM methods can be categorized generally as either mathematical model-based or data-driven [5–7]. The mathematical model-based methods include knowledge of the basic principles of the object under inspection, such as material properties and structural features [8,9], whereas data-driven methods extract the information from the empirical data, to predict the health of a certain component or system [10,11]. With the easy availability of industrial data of different components and systems, data-driven methods, including DL and ML, are gaining popularity among PHM applications.

In particular, DL is considered to be well equipped in providing solutions for issues such as large-scale data processing [12] and the automatic derivation of meaningful features [13], as well as transferring knowledge between operating conditions and results. As many researchers have applied DL to PHM applications, they have significantly focused on fault diagnosis or prognosis [14,15], while others focus on applications to a specific item, such as a bearing or electronic system [16–18]. However, when it comes to commercialization and real-time implementation of DL methods, computational cost becomes much higher than typical ML methods, because of the huge volume of data involved in the extensive feature extraction and learning process. In a recent study published by MIT (Massachusetts Institute of Technology) [19], the computational limits of DL were analyzed, resulting in a claim that the computational requirements of DL have escalated rapidly. This increase in computational power became critical to enhancing performance. The authors raised concerns that if the present development persists, these computational criteria will soon become prohibitive both technically and economically. The study indicated that DL development would be restricted by its evaluation metrics and that the

ML society would either improve the performance of DL significantly or switch to more efficient ML techniques.

On the other hand, ML has achieved equally significant results. It was effectively used to solve the problems related to clustering, regression, classification, or data dimensionality reduction [20]. ML has demonstrated its tremendous capabilities in a variety of ways. ML was used to develop several useful systems such as the Go-playing system [21], cars with the self-driving ability [22], and image classification [23]. As a result, various aspects of our everyday life are driven by ML algorithms, such as image and speech recognition [24,25], website searching [26], fraud detection [27], email segregation [28], credit count [29], and many more. Data obtained from a computer by different sensors under varying operating conditions are the basis of ML-based fault detection and diagnosis systems. The output of the sensors is generally time series. Features are normally derived using an analysis scheme based on time, frequency, or time-frequency domain analysis. The techniques for studying the frequency domain encompass envelope analysis [30] and high-order spectral analysis [31]. Whereas, techniques for the time-domain analysis include root mean square, high-order statistics, and short-time impulse [32,33]. Time-frequency domain analysis techniques include Hilbert–Huang, short-time Fourier, and wavelet transforms [34,35]. ML's key challenge is the tedious and time-consuming process of manually extracting features that require expert knowledge. ML-based classifier might be less accurate than DL without proper discriminant feature extraction and selection. However, if the extraction and selection of the features are performed correctly with knowledge about the type of input data being utilized, greater classification accuracy can be achieved.

Subsequently, several methods for fault detection and diagnoses, such as vibration analysis [36–38], electromagnetic field monitoring [39], MCSA analysis, chemical analysis, infrared signal analysis [40–43], and partial release measurement, have been examined. These fault detection and diagnosis methods are specifically limited to detect the electrical and mechanical faults related only to the electric motor. In an industrial environment, the robots use electric motors coupled with some mechanical parts, such as rotate vector (RV) reducer. This is an additional mechanical part rather than an integral motor part, conjoined with the electric motor to increase or decrease the speed of rotation (rpm). The performance of these reducers degrade over time, and cause the robotic system to work less efficiently with greater power consumption. Normally this happens due to damaged gears inside of the reducer caused by misaligned or cracked teeth. Previously, this type of reducer fault was detected through different procedures, among which the most common use vibration signal analysis, ferrography, or acoustic emission analysis. While vibration analysis has frequently been used, it requires the use of costly vibration sensors. Furthermore, it is difficult to place and install sensors in specific locations to record the vibration signals. The surrounding environment can also create noise, rendering the sensor readings inaccurate. As an alternative, MCSA has several advantages over vibration analysis. MCSA uses the motor control unit's embedded current signal, requiring no additional sensors, which results in low cost, and a less complex system. In addition, the current signals are unique, and are not easily affected by the surrounding working environment. The problem with implementing MCSA for reducer fault detection and diagnosis is that the reducer is not considered an integral part of the electric motor, making it hard to implement such a technique to distinguish a faulty state. MCSA is typically used to detect faults related to an electric motor. However, in this work we utilize the classification abilities of ML-based classifiers, and present a holistic feature selection and feature extraction approach that is integrated with MCSA, to detect and diagnose the faults related to the RV reducer for a component-level PHM. Using the proposed methodology, the complexity involved in handling vibration signals for such type of fault will be eliminated, and faults can be detected using only the three-phase electric current of the motor. When it comes to real-time implementation, the fault detection system will have a fast response with less computational time (compared to DL). The sensing components will be enormously reduced, which will effectively decrease the cost of the overall system. Besides, we analyze the procedures involved in developing such kinds of systems in real-time, and present practical results obtained using an industrial robot.

This paper is divided into the following sections: Section 1 provides an introduction, while Section 2 describes the materials and methods used. Section 3 then presents the results and discussion, and finally, Section 4 concludes the study.

2. Materials and Methods

The experimental test bench used in this study has three key components: (1) the Hyundai Robot YS080, (2) a controller device, and (3) a personal computer (PC). Figure 2 shows the components of the experimental test bench. The proposed method is implemented on an industrial robot developed by Hyundai Robotics. The robot model is YS080 and has a maximum payload capacity of 80 kgf. The robot consists of six joints or axes. Each axis is equipped with an electric motor of different specifications. With the help of electromechanical couplings, the robot can rotate 360 degrees along each axis. Consequently, at each axis, the electric motors are coupled with reducers to increase or decrease rotational speed. Figure 3 shows (a) the basic free-body diagram, and (b) an actual image of the Hyundai Robot, YS080, identifying the six joints.

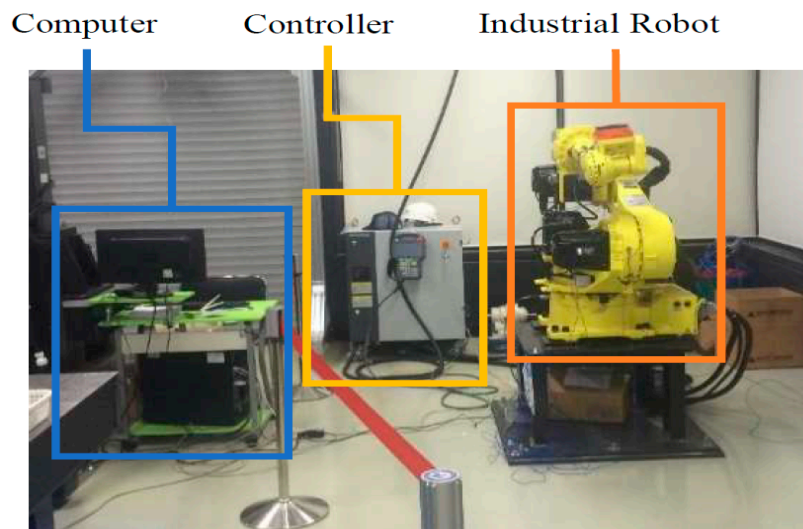


Figure 2. Components of the experimental test bench.

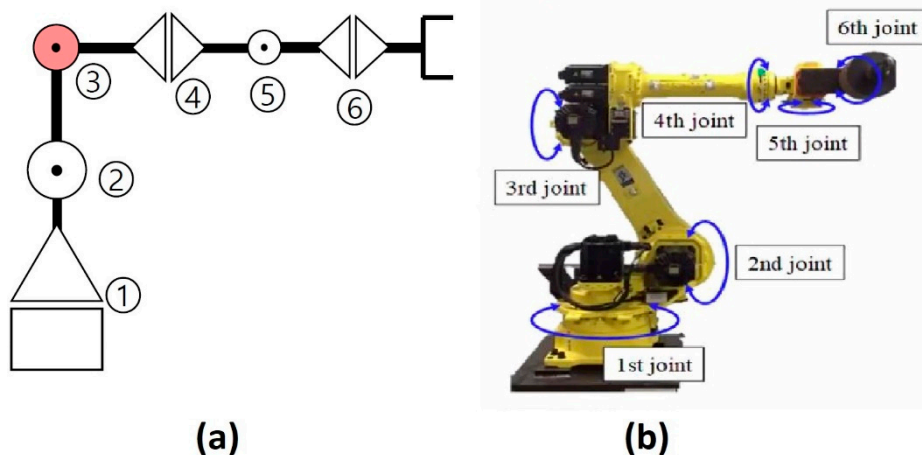


Figure 3. (a) Free-body diagram, and (b) actual Image of the Hyundai Robot YS080.

The three-phase servo motors are mounted on each axis. The motors with different specifications are mounted based on the amount of mechanical load that each axis holds. Axes 1, 2, and 3 are composed of motors with electrical power higher than those of axes 4, 5, and 6. The motors have different rotational speeds and frequencies. Table 1 summarizes the specifications of the electric

motors on each axis. These electric motors are controlled by a controller device that is comprised of three-phase servo motor drivers. The controller is further connected to a personal computer (PC) to send commands to the robot to execute different types of tasks.

Table 1. Specifications of the electric motors.

Axes No.	Power (kW)	Speed (rpm)	Voltage (V)	Current (A)	Frequency (Hz)
1, 2, 3	5.9	2000	200	25.1	166
4, 5, 6	2	3000	200	11.7	250

2.1. The Architecture of the Proposed Methodology

Figure 4 shows the basic flow chart of the proposed fault detection and diagnosis methodology for the RV reducer based on MCSA with ML-based classification:

The proposed method is divided into the following steps:

1. Data acquisition
2. Data-preprocessing
3. Signal analysis
4. Deterministic analysis
5. Classification

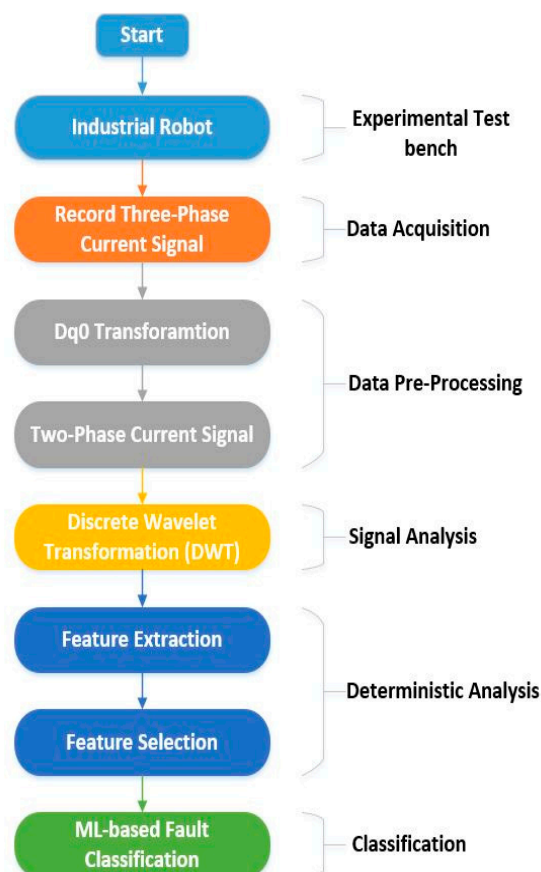


Figure 4. A flowchart of the proposed methodology.

To implement the proposed method, an experimental test bench based on an industrial robot was used. Initially, the data are recorded employing current sensors installed at each of the electric motors' three-phases. Data are recorded for each motor installed at a specific point of the industrial robot. The current signals data in three-phase is pre-processed, and data dimension reduction is performed

to compress the data. The data dimension is reduced using the DQ0 transformation. The DQ0 transformation converts the three-phase current signals to two-phase current signals, without losing any useful information. Using discrete wavelet transform (DWT), the two-phase current signals are further analyzed in the time-frequency domain. DWT breaks down the signals into wavelets, which are further used to extract features. Several features are extracted from the wavelets based on wavelet characteristics and statistics. Then, these features are analyzed using feature selection algorithms to select the most prominent and deterministic features. Upon determining the prominent features among the extracted features, ML-based classifiers are trained to categorize among the various classes of faults. A detailed description of each step is given in the subsequent subsections.

2.1.1. Data Acquisition

For MCSA, the motor current signals were recorded for each of the three phases of the electric motor using current sensors. Figure 5 shows the basic block diagram of the data acquisition process for one axis motor. The current sensors used for this purpose were the Hall Effect Base Linear Current Sensors WCS6800. The current sensors are installed on each phase of the electric motors, i.e., 18 current sensors in total to record 18 current signals for 6 electric motors. The current signals for each axis motor are recorded using NI DAQ 9230 modules. This data acquisition module sends the recorded data to a PC with LabView installed on it. The received signals are analyzed, and a final database comprising of the signal information for each axis motor's three-phase current signals is formed.

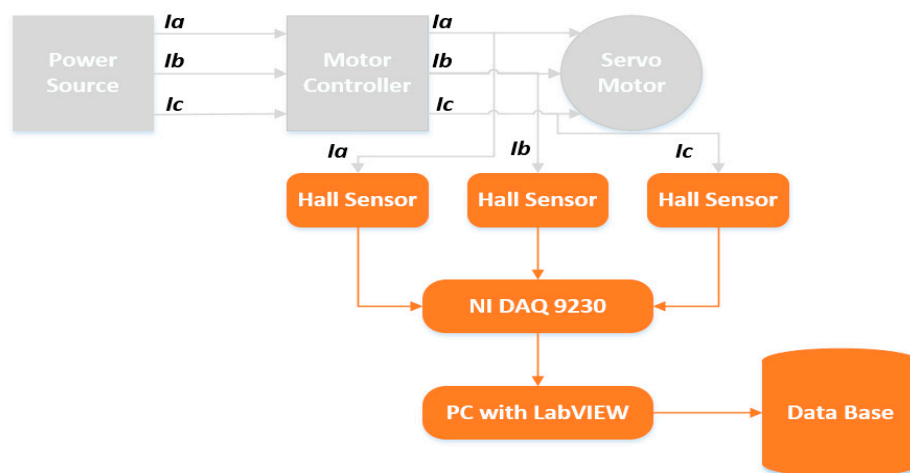


Figure 5. Basic block diagram of the data acquisition process for one axis motor.

The data are recorded simultaneously for each motor under different fault scenarios. In the first scenario, an RV reducer eccentric bearing fault was inserted in the reducer coupled with the 4th axis motor. In the second scenario, the fault was inserted by replacing the RV reducer with a deteriorated one. The data were recorded for a total of three classes: normal, faulty (RV reducer eccentric bearing fault), and faulty_aged (RV reducer aging fault). Figure 6 shows the location of the fault in the Hyundai Robot with a detailed conceptual view. Figure 7 shows the fault modes with an example of a fault specimen. The robot was made to operate in all directions along each axis of rotation for several cycles. One cycle refers to the completion of one range of motion along one axis. The data were recorded for 10 cycles for each axis. Subsequently, the motors were operated at different speed profiles ranging (10 to 100) % of the rated speed to observe the effect of the change on the speed of fault detection and diagnosis system. Figure 8 shows the details of the equipment used in the data acquisition process. The data are recorded for each axis motor, even though the fault is just inserted into the RV reducer at axis 4, since due to mechanical coupling, a fault in the one axis might affect the operation and efficiency of the other axis motors.

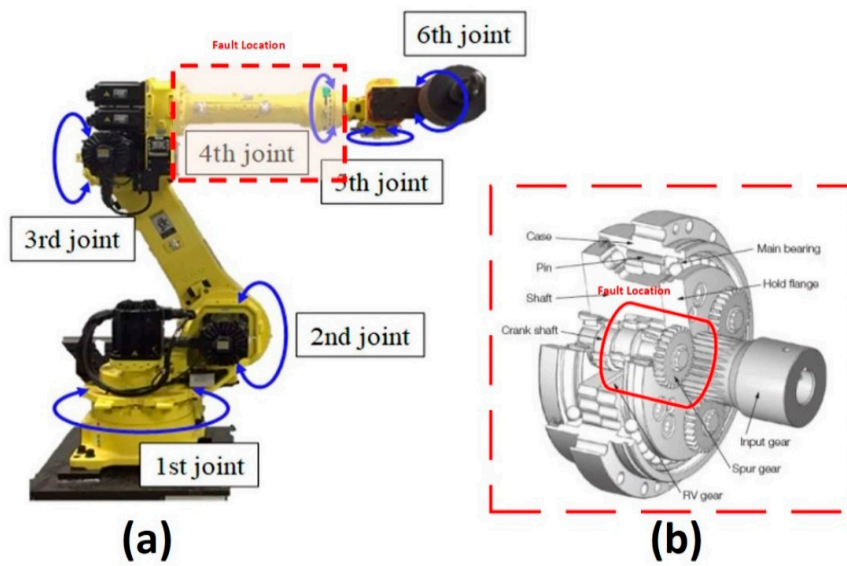


Figure 6. Location of the fault: (a) Hyundai Robot, and (b) Detailed conceptual view.

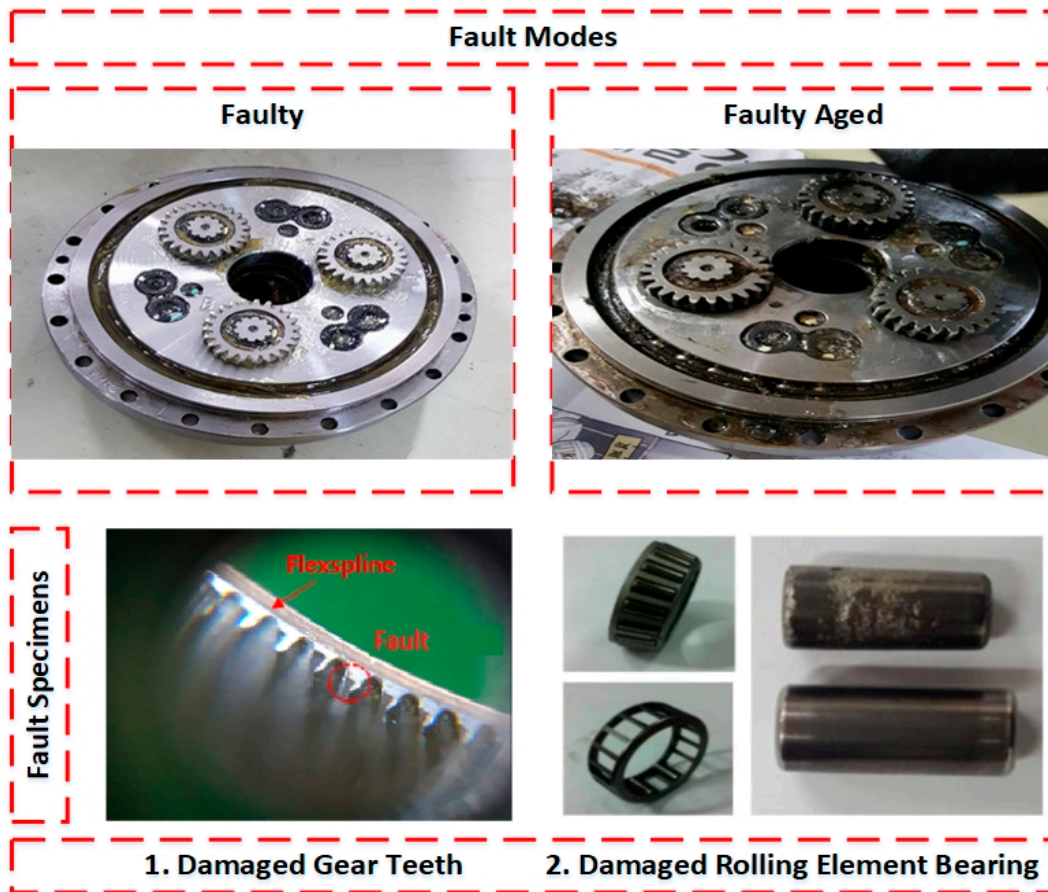


Figure 7. Fault modes and an example of a fault specimens.

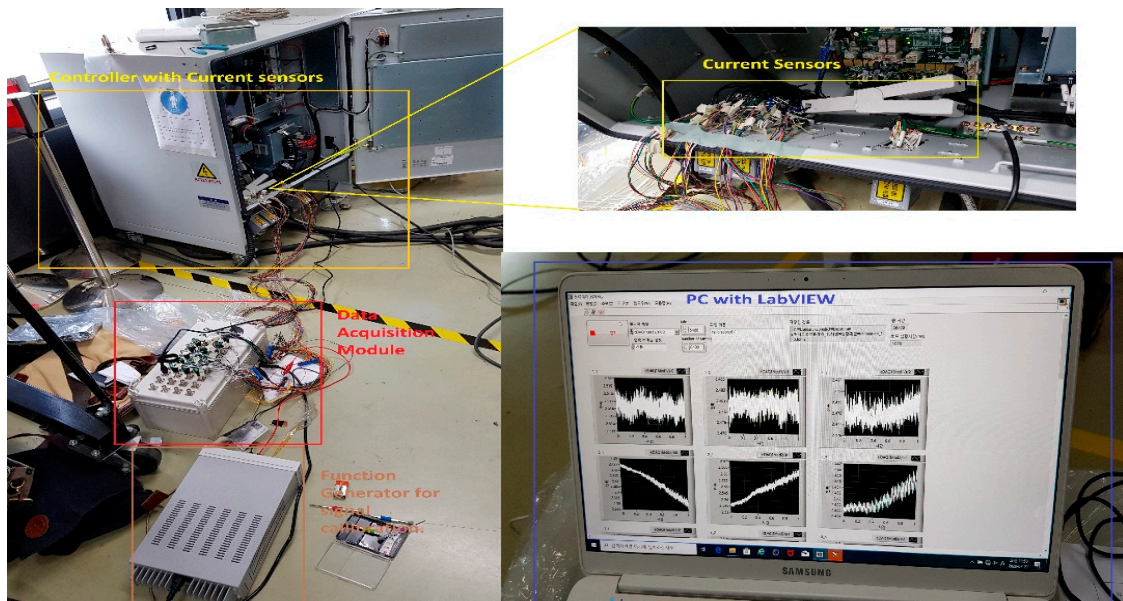


Figure 8. The equipment used in the data acquisition process.

2.1.2. Data Pre-Processing

The recorded data were pre-processed to reduce the dimension in such a way that the useful information from the obtained three-phase current signals would not be missed. The data dimension reduction is performed to make the data compression compact, and more manageable. The DQ0 transformation was used for this purpose. The DQ0 transformation is a well-proven technique for dimensional reduction, converting a three-phase current signal to a DQ0 rotating reference frame. This transformation projects the information from a 3D space to a 2D space, without any loss of information. For the sinusoidal balanced signal, the projected signal describes a circle in the projected plane. This simplifies the frequency estimation, since the circle simply corresponds to the analytic signal. The transformation preserves the amplitude of the electrical components (such as voltages and currents), and is widely used in electrical engineering to implement and design the control parameters of an electric motor. Figure 9 shows the signal representation of (a) three-phase, and (b) 2D, DQ transformation. Figure 10 shows the conceptual representation of the three-phase (abc) and (DQ0) reference frames.

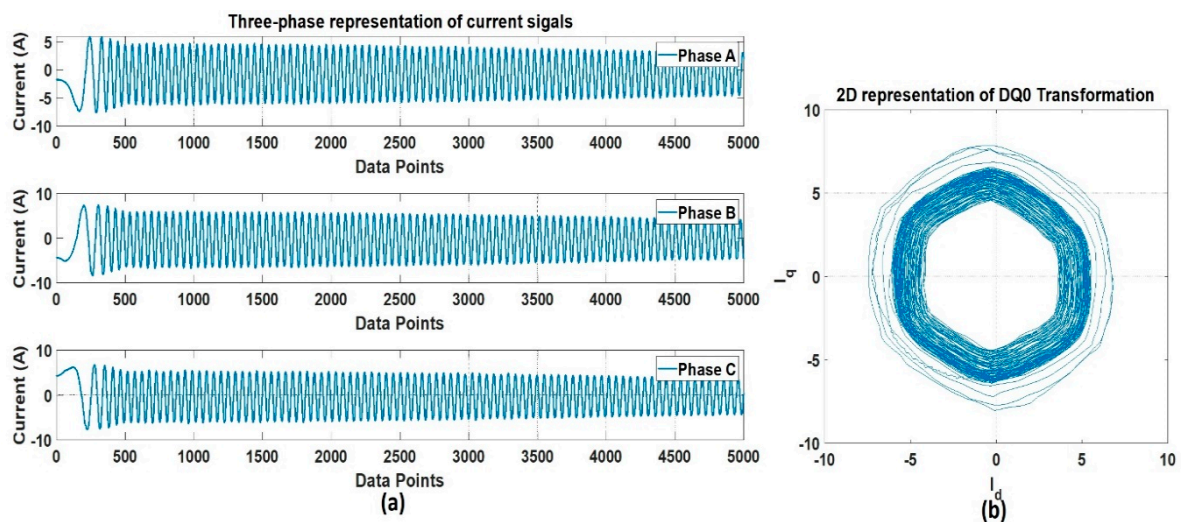


Figure 9. The current signal representation: (a) Three-phase, and (b) 2D representation of DQ transformation.

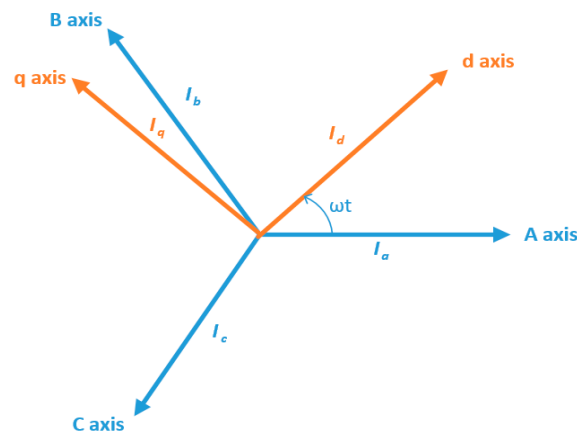


Figure 10. Conceptual representation of three-phase (abc), and DQ0 reference frames.

There are two types of DQ0 transformations: cosine-based, and sine-based. Cosine-based transformation aligns the rotating DQ frame with A-axis at $t = 0$, and results in $d = 0$, $q = -1$, $zero = 0$. Sine-based transformation aligns the rotating DQ frame 90 degrees behind A-axis at $t = 0$, and results in $d = 1$, $q = 0$, $zero = 0$. Both of these transformations differ in the aligned reference axis. In the cosine-based transformation, the d-axis is aligned with the A-axis, whereas in the sine-based transformation, the q-axis is aligned with the reference A-axis. When it comes to data dimensionality reduction, the results for each case are similar. Therefore, in this work, we utilized the sine-based transformation given in Equation (1):

$$T_{abc-dq} = \sqrt{\frac{2}{3}} \begin{bmatrix} \sin \omega t & \sin \left(\omega t - \frac{2\pi}{3} \right) & \sin \left(\omega t + \frac{2\pi}{3} \right) \\ \cos \omega t & \cos \left(\omega t - \frac{2\pi}{3} \right) & \cos \left(\omega t + \frac{2\pi}{3} \right) \\ \frac{1}{\sqrt{2}} & \frac{1}{\sqrt{2}} & \frac{1}{\sqrt{2}} \end{bmatrix} \quad (1)$$

2.1.3. Signal Analysis

The signals extracted from the sensors are stored in a database. Signal analysis is performed to analyze the pattern, and the difference between normal and faulty conditions. Signal analysis is the most important step of any fault detection and diagnosis. Different kinds of analysis schemes are developed for this purpose. These schemes can be categorized into time-domain, frequency-domain, and time-frequency domain analyses. In the time-domain analysis, statistical features summarizing the useful information in the time-domain are extracted from the signal [44–46]. On the other hand, frequency-domain analysis is believed to work well in distinguishing some faults with certain characteristics. Fourier transform is the most commonly used tool for frequency-domain signal analysis. It breaks down a time waveform into its frequencies. Fast-Fourier Transform (FFT) is commonly used for the study of time continuum signals. This transform utilizes the spectral frequency analysis scheme. At a certain frequency, the signature of a fault may be a high degree of vibration. When it comes to the processing of non-stationary signals (typically in machine faults), the time, and frequency domain analysis have specific limits. Time-frequency domain analysis, a blend of frequency and time domains, has been developed to address these limitations [47]. A typical method used for this purpose is called the short-time Fourier transform (STFT) [48], which divides the entire waveform signal through short-time windows and Fourier transforms into several segments. Another common approach with a similar aim is wavelet transformation. Wavelet Transform is an analytical method that uses a definition of spectral decomposition by the scaling concept for time-varying or non-static signals. Of the many techniques in the past that have been developed for different signal-processing applications, wavelet theory offers a dedicated and compact framework [49,50]. Multi-resolution signal

analysis with a good time- and the frequency-localization mechanism is one of its several features. It is effective for both stationary and nonstationary signal processing. The most commonly used method among the wavelet transform is the discrete wavelet transform (DWT). In numerical and functional analyses, a discrete transform wavelet (DWT) is a transform that discretely samples the wavelets. In comparison to the other wavelet transforms, a crucial advantage it has over Fourier transforms (frequency-domain analysis) is temporal resolution, capturing both frequency and location information (location in time). Therefore, in this work, we selected time-frequency domain analysis using DWT to analyze the signals recorded under different fault conditions. Figure 11 shows the decomposition tree of the recorded current signals. The three-phase current signals I_{abc} are pre-processed using DQ0 transformation. The output of the Dq0 transformation is a two-phase signal I_{dq} in the d-axis and q-axis. This two-phase signal is decomposed into wavelets using DWT.

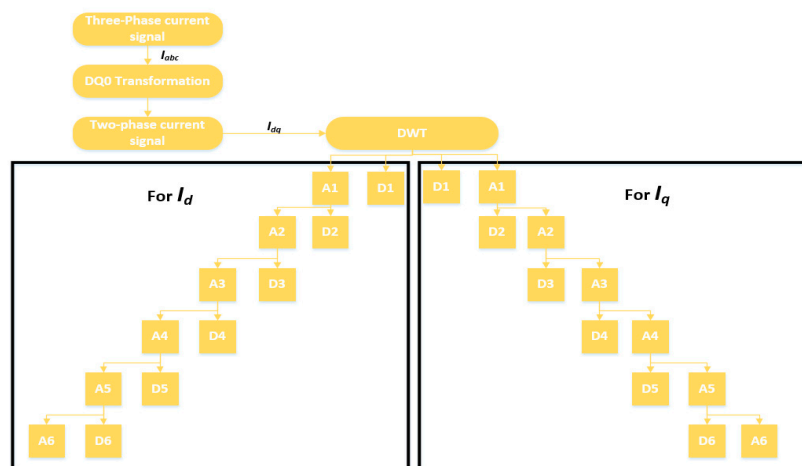


Figure 11. Signal decomposition tree.

Considering $I_d[n]$ and $I_q[n]$ as the original signal sequence, after the convolution with h and g quadrature mirror filters, the signal sequence is decomposed into the approximation $A_1[n]$ and detail components $D_1[n]$ at level 1. Then, the approximation component $A_1[n]$ is further decomposed into $A_2[n]$ and $D_2[n]$ at the next level. This process is repeated until a desired level of decomposition is achieved. Mathematically, it can be represented by Equations (2)–(5):

$$A_m[n] = \sum_{k=-\infty}^{\infty} g[n-k]I_d[k] \quad (2)$$

$$D_m[n] = \sum_{k=-\infty}^{\infty} h[n-k]I_d[k] \quad (3)$$

$$A_m[n] = \sum_{k=-\infty}^{\infty} g[n-k]I_q[k] \quad (4)$$

$$D_m[n] = \sum_{k=-\infty}^{\infty} h[n-k]I_q[k] \quad (5)$$

where, m , n , and k represent the scale of decomposition, sample points, and translation coefficients, respectively. There are several types of the wavelet transform, but among them all, the most widely used series of discrete wavelet transforms was developed by the Belgian mathematician Ingrid Daubechies in 1988. The Daubechies wavelet transform is based on the use of the recurrence relationships to yield increasingly fine and distinct samples of an implicated mother wavelet function [51,52]. In this work, we focus on using 6-level Daubechies wavelets. Levels are selected by observing the decomposition state of the signal at different levels.

2.1.4. Deterministic Analysis

Upon implementing the DWT on the DQ0 transformed current signals, several features were extracted from the decomposed wavelet signals. The feature extraction and selection is the most important part of any fault detection and diagnosis system. Especially when it comes to the ML, improper feature extraction and selection can cause poor classification accuracy. As mentioned in the introduction section of the manuscript, ML's key challenge is its tedious process of manual feature extraction. ML-based classifier might be less accurate than DL without proper discriminant feature extraction and selection. However, if the extraction and selection of the features are performed correctly with the knowledge about the type of input data being utilized, greater classification accuracy can be achieved.

In this work, we adopt an approach where we extract two types of features from the decomposed wavelets of the original current signals. The first type of features are solely based on the wavelet characteristics, and focus on the wavelet domain, whereas the second type of features are extracted based on statistical analysis. The reason for extracting different types of features is that in typical analysis methodologies, either the first type of feature is utilized, or the second type. Also, it is dependent on the type of fault being diagnosed. In the case of RV reducer fault detection and diagnosis, due to the high sensitivity of the fault, the typical feature extraction methodologies fail to provide higher classification accuracy. Therefore, we developed a method where we extract features based on both of the above-mentioned types, and implement deterministic feature selection to choose the most prominent features among them. Doing so provides the power to utilize the properties of wavelet and statistical domain simultaneously in an efficacious way. We name these two types as (1) wavelet specific features, and (2) wavelet-based statistical features. Wavelet specific features extracted from wavelets are the wavelet energy and Shannon wavelet entropy. Wavelet-based statistical features extracted from wavelets are the mean, standard deviation, variance, kurtosis, and skewness. Tables 2 and 3 define the wavelet specific features and wavelet-based statistical features, respectively.

Table 2. Definition of Wavelet Specific Features.

Feature	Definition
Wavelet Energy	$Energy (D_i) = \sum_{j=1}^N D_{ij} ^2$
	$Energy (A_i) = \sum_{j=1}^N A_{ij} ^2$
Shannon Wavelet Entropy	$Entropy (s) = s_i^2 \log(s_i^2)$

Table 3. Definition of Wavelet-based statistical features.

Feature	Definition
Mean	$\mu = \frac{1}{N} \sum_{i=1}^N n_i$
Standard Deviation	$STD = \sqrt{\frac{1}{N} \sum_{i=1}^N (n_i - \mu)^2}$
Variance	$VAR = \sqrt{\frac{1}{N-1} \sum_{i=1}^N (n_i - \bar{n})^2}$
Kurtosis	$KRT = \frac{\sum_{i=1}^N (n_i - \mu)^4}{(N-1)\sigma^4}$
Skewness	$SKW = \frac{\sum_{i=1}^N (n_i - \mu)^3}{(N-1)\sigma^3}$

In Tables 2 and 3, D_i and A_i are the detail and approximation components of the i_{th} level decomposed signal, respectively; s is the input signal, and s_i is the coefficient of s an an orthonormal basis; n is the value of one observation, and N is the number of observations. We extracted the features from each detail coefficient ($D1$ to $D6$) for both the I_d and I_q components of the current signal. A total of 24 wavelet specific features and 60 wavelet-based statistical features were extracted. Tables 4 and 5 show the details of the extracted features. These extracted features were further passed through some feature selection algorithm based on the correlation analysis and chi-square tests to reduce the number of features. The features with prominent patterns were distinguished and used for the classification of the faults. Figure 12 shows the flow chart of the feature selection scheme.

Table 4. Detail of the extracted wavelet specific features.

Wavelet Specific Features	D1	D2	D3	D4	D5	D6
I_d	Energy_Id_D1	Energy_Id_D2	Energy_Id_D3	Energy_Id_D4	Energy_Id_D5	Energy_Id_D6
	Entropy_Id_D1	Entropy_Id_D2	Entropy_Id_D3	Entropy_Id_D4	Entropy_Id_D5	Entropy_Id_D6
I_q	Energy_Iq_D1	Energy_Iq_D2	Energy_Iq_D3	Energy_Iq_D4	Energy_Iq_D5	Energy_Iq_D6
	Entropy_Iq_D1	Entropy_Iq_D2	Entropy_Iq_D3	Entropy_Iq_D4	Entropy_Iq_D5	Entropy_Iq_D6

Table 5. Detail of the extracted wavelet-based statistical features.

Wavelet-Based Statistical Features	D1	D2	D3	D4	D5	D6
I_d	Mean_Id_D1	Mean_Id_D2	Mean_Id_D3	Mean_Id_D4	Mean_Id_D5	Mean_Id_D6
	STD_Id_D1	STD_Id_D2	STD_Id_D3	STD_Id_D4	STD_Id_D5	STD_Id_D6
	VAR_Id_D1	VAR_Id_D2	VAR_Id_D3	VAR_Id_D4	VAR_Id_D5	VAR_Id_D6
	KRT_Id_D1	KRT_Id_D2	KRT_Id_D3	KRT_Id_D4	KRT_Id_D5	KRT_Id_D6
	SKW_Id_D1	SKW_Id_D2	SKW_Id_D3	SKW_Id_D4	SKW_Id_D5	SKW_Id_D6
I_q	Mean_Iq_D1	Mean_Iq_D2	Mean_Iq_D3	Mean_Iq_D4	Mean_Iq_D5	Mean_Iq_D6
	STD_Iq_D1	STD_Iq_D2	STD_Iq_D3	STD_Iq_D4	STD_Iq_D5	STD_Iq_D6
	VAR_Iq_D1	VAR_Iq_D2	VAR_Iq_D3	VAR_Iq_D4	VAR_Iq_D5	VAR_Iq_D6
	KRT_Iq_D1	KRT_Iq_D2	KRT_Iq_D3	KRT_Iq_D4	KRT_Iq_D5	KRT_Iq_D6
	SKW_Iq_D1	SKW_Iq_D2	SKW_Iq_D3	SKW_Iq_D4	SKW_Iq_D5	SKW_Iq_D6

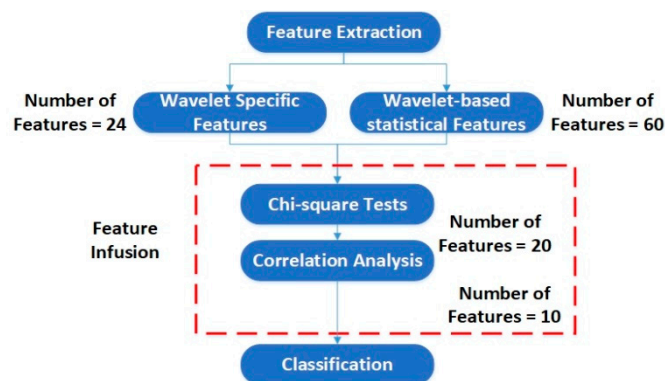


Figure 12. Flowchart of the feature selection scheme.

3. Results and Discussion

Figure 13 shows the recorded waveforms of the current signals for each axis. The current signals were recorded by operating each axis motor. The data were recorded for 10 cycles of rotation. For the sake of simplicity, only one cycle's data are presented. Figure 14 shows the recorded waveform when only the 4th axis motor was operating.

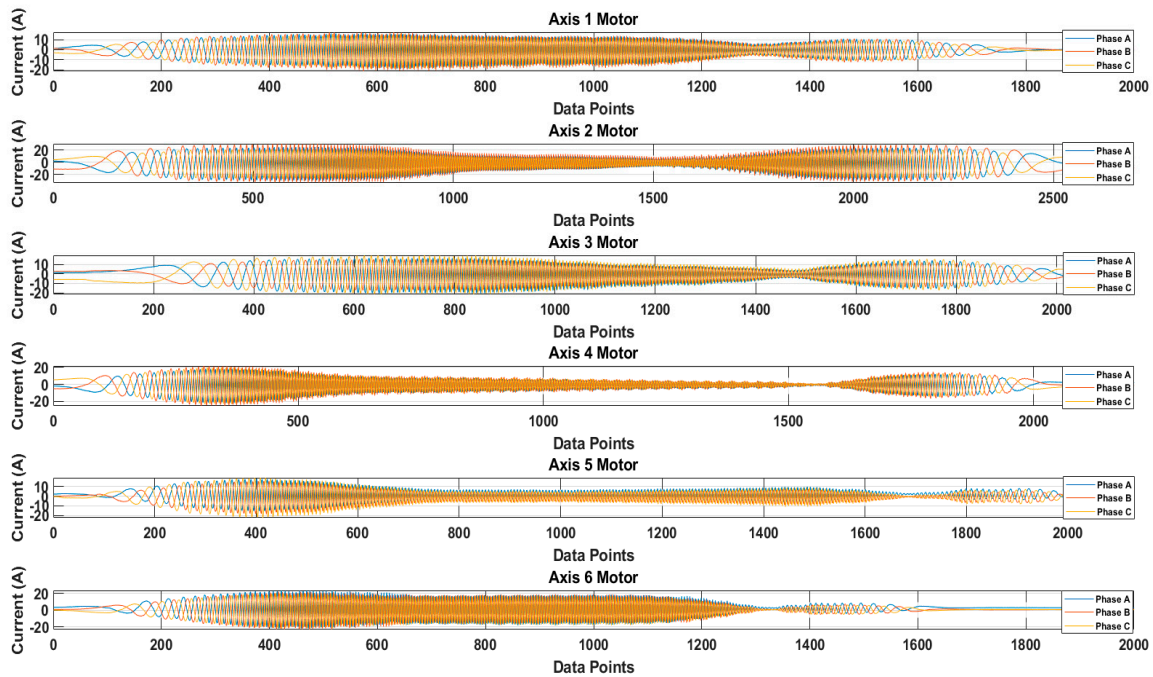


Figure 13. Recorded waveforms of the three-phase current signals for each axis motor.

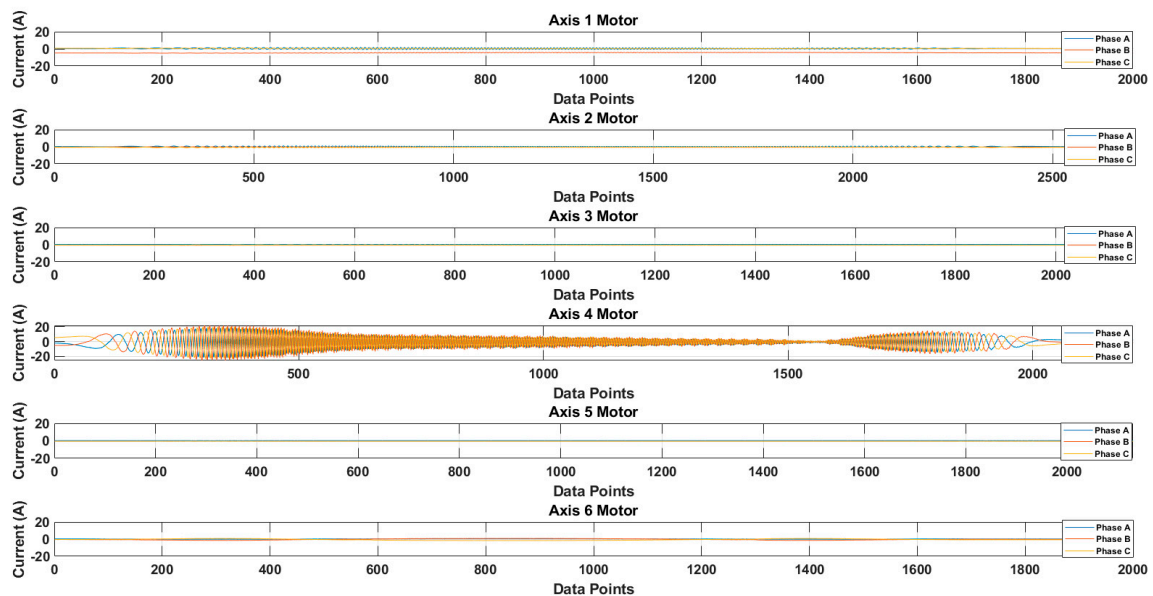


Figure 14. Recorded waveforms for single-axis motor operation.

It is possible that because of the mechanical couplings between each axis of the robot, during the normal and faulty states, the operation of one axis motor might affect the other axis motors, leading to simultaneous current signature analysis. In the simultaneous current signature analysis, the current signals of all motors should be analyzed, regardless of the fault location. This leads to more complex fault detection and diagnosis system, but upon several experimental findings with the results presented

in Figure 14, it is clear that for a robotic arm like the Hyundai Robot, the mechanical couplings along the robotic arm do not affect the current signals of another motor. This gives the possibility of focusing on only single-axis current signature analysis. In case there is some fault in an axis, only that axis current signature analysis would be enough to distinguish the fault, without the worry of the mechanical relation between the different axes of the robot. Based on this and the fault location (RV reducer of the 4th axis), we focused only on the 4th axis current signature analysis. We recorded the current signals for the 4th axis motor under three different fault scenarios: normal, faulty (RV reducer eccentric bearing fault), and faulty_aged (RV reducer aging fault). Figure 15 shows the three-phase current signal for the 4th axis motor under normal, faulty, and faulty_aged scenarios. These three-phase current signals were converted to two-phase using DQ0 transformation to achieve the reduced data dimensions. Figure 16 shows the DQ0 transformed two-phase current signals for the 4th axis motor under each fault scenario.

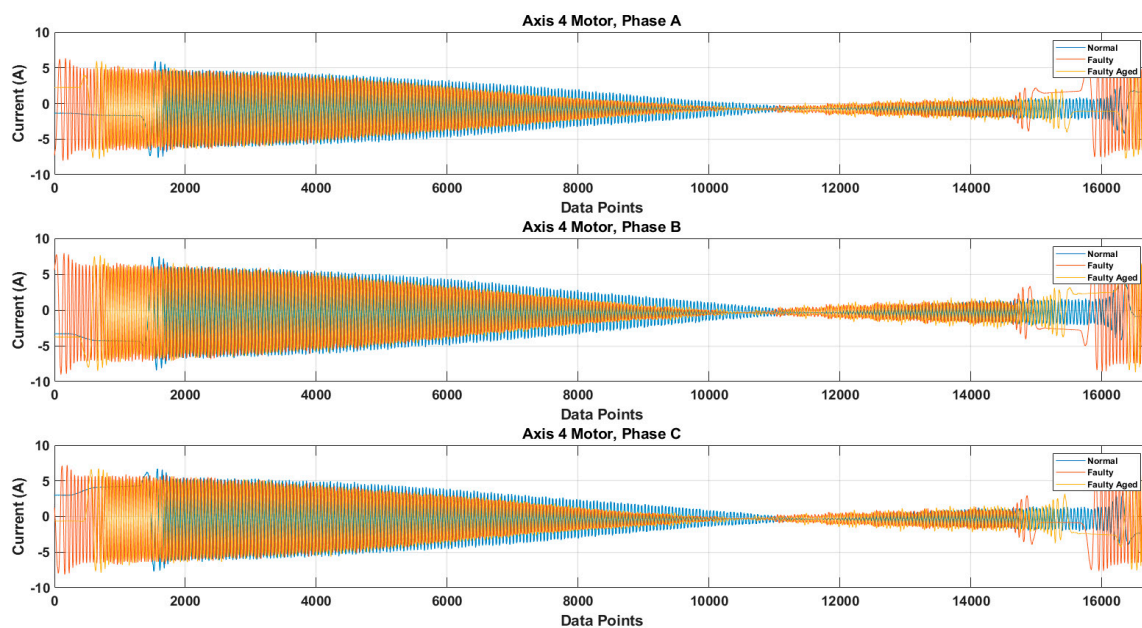


Figure 15. Three-phase current signal for 4th Axis motor under Normal, Faulty, and Faulty_Aged scenario.

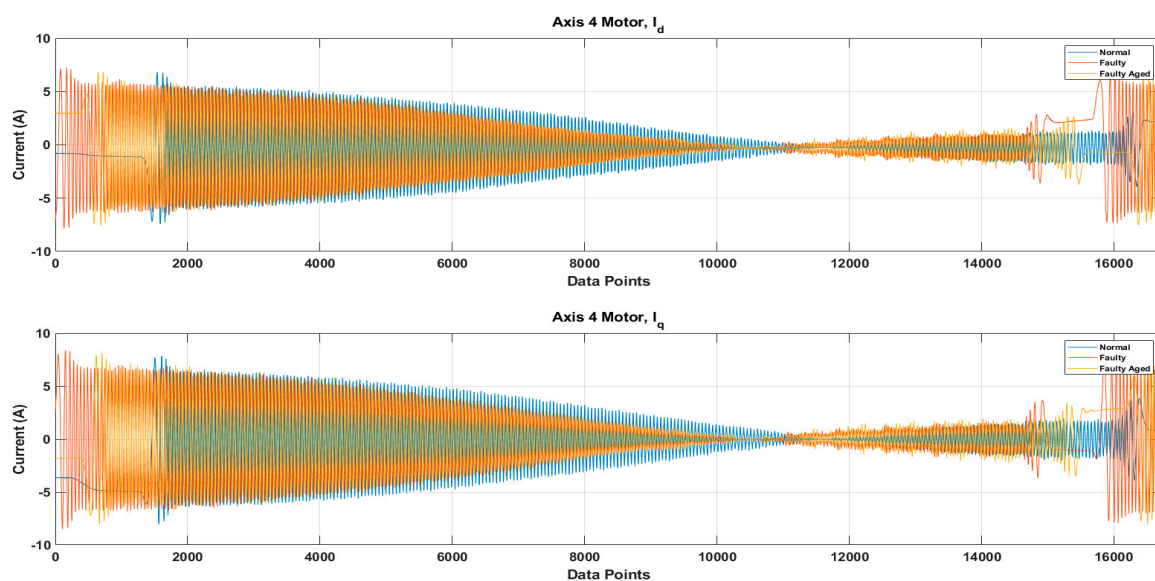


Figure 16. The DQ0 transformed two-phase current signals under Normal, Faulty, and Faulty_Aged scenario.

The RV reducer fault is a mechanical fault, and if all the operating parameters, such as speed, frequency, amplitude, and signal shape, are not considered properly, the use of MCSA for the detection of such kind of fault can be a complicated task. Normally, when it comes to the detection of electrical and electronic faults related to electric motors and their controller devices, the response of the current signal shows a similar pattern under different operating parameters, due to which it becomes easy to detect the fault by just observing the current signal response with selected parameters [53–55]. However, in the case of RV reducer, due to the fault nature and electromechanical relation between the motor and reducer, it would be hard to achieve higher accuracy if a fault detection and diagnosis system is not developed with consideration of all the operating parameters. Among these parameters, the speed of the rotation of the motor is the most important parameter, due to its direct relation to the reducer device. Considering this factor, we recorded the data for different operating speeds of the motor, to observe the effect of speed change in each fault scenario. We selected a speed profile where we recorded the signal response of the motor at the speed range (10 to 100) % of the rated speed. This gave us an overall view of the faults. We present the current signal response for the speed of 20%, 60%, and 100%. Figure 17 shows the DQ0 transformed current signal for each fault scenario under 20%, 60%, and 100%. It can be observed that with the increase in the rotation speed of the motor (rpm), the amplitude, frequency, and mechanical rotational speed of the robot along the axis also increase. In Figures 13–16, the rpm was 10% of the rated speed. In Figure 17, one mechanical cycle corresponds to the mechanical rotation of the robot along each axis. The robot moves clockwise (CW) to complete one cycle, and returns to its starting position by moving counterclockwise (CCW). With the increase in the rpm of the motor, the mechanical cycles of the robot also increase.

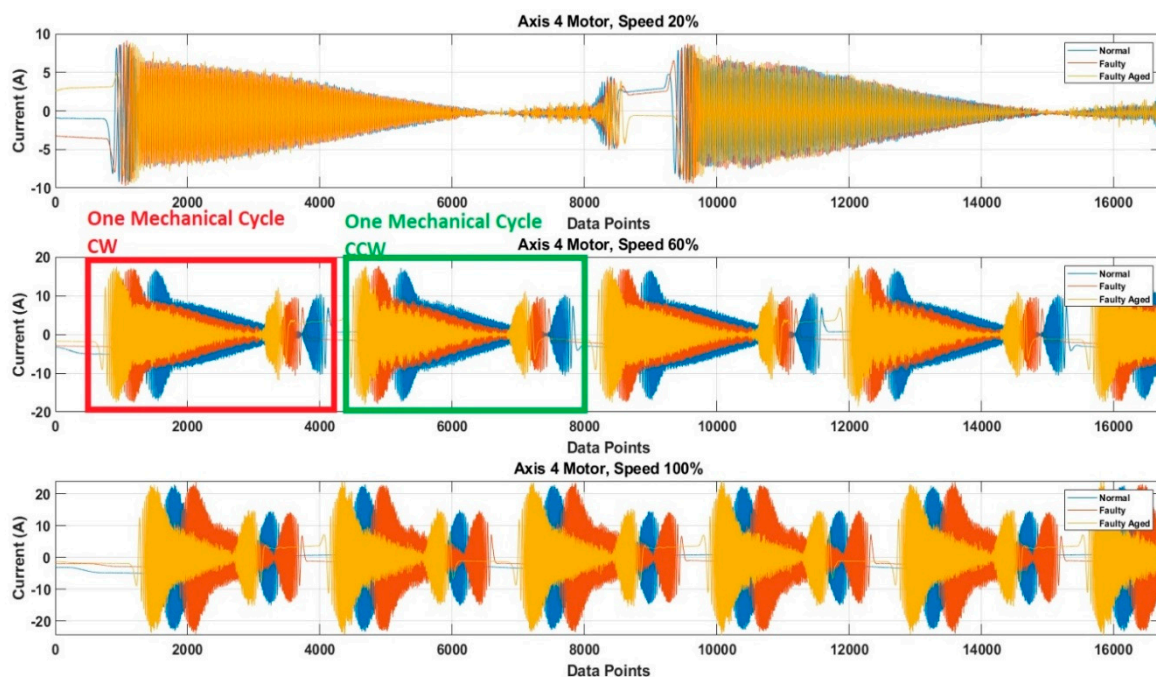


Figure 17. The DQ0 transformed current signal for each fault scenario under (20, 60, and 100) %.

After data acquisition and DQ0 transformation, we implemented DWT on components I_d and I_q of the current signal for all fault scenarios. The selection parameters, including the sampling frequency and the number of samples, should be carefully selected to achieve the right resolution for wavelet analysis. Few restrictions have been taken into account for this, including (1) signal bandwidth, (2) wavelet spectral band decomposition, (3) frequency resolution, and (4) acceptable level of decomposition. The use of the Shannon theorem provides a minimum sampling frequency of 1000 Hz. Equation (6) gives the total number of samples, N_s , required for an already given resolution R [20–22].

$$N_s = \frac{f_s}{R} \quad (6)$$

In our case, for the resolution of $R = 0.1$ Hz, we chose a sampling frequency $f_s = 12.8$ kHz. Hence, $N_s = 128,000$ samples were acquired. Figures 18 and 19 show the output results of the DWT for I_d and I_q components of the current signal at a speed of 100% without any fault, whereas Figure 20 shows a detailed view of the $D6$ decomposed wavelet coefficient for each fault scenario. In these figures, s is the original signal, a is the approximation coefficient, and d is the detail coefficient extracted by the decomposition of the original current signal using six-level Daubechies wavelets.

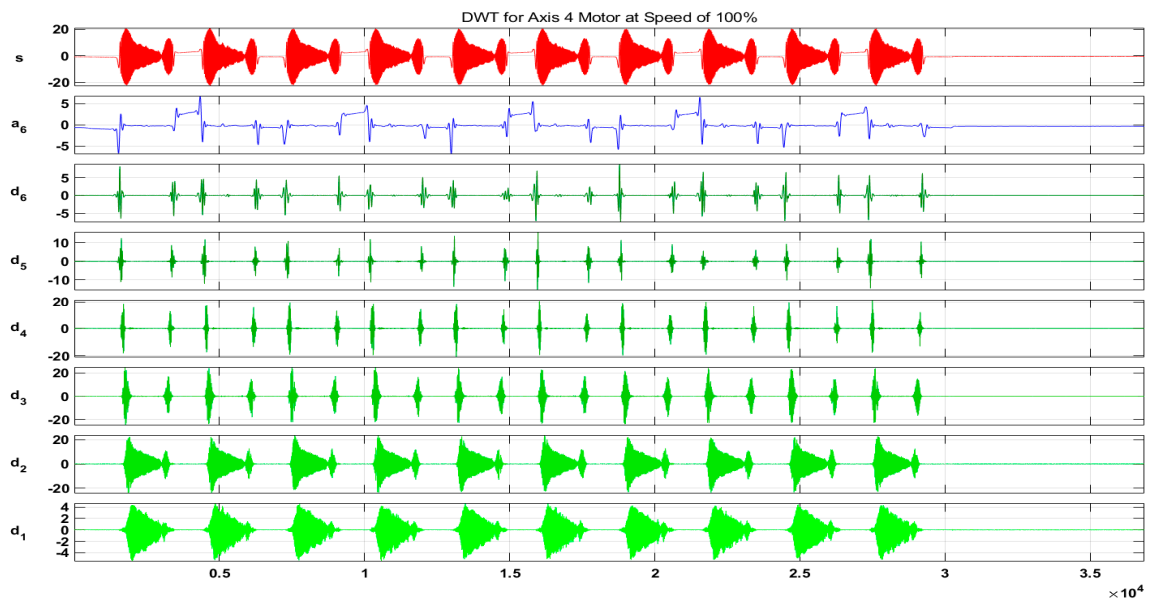


Figure 18. Output results of the DWT for I_d component of the current signal at a speed of 100%.

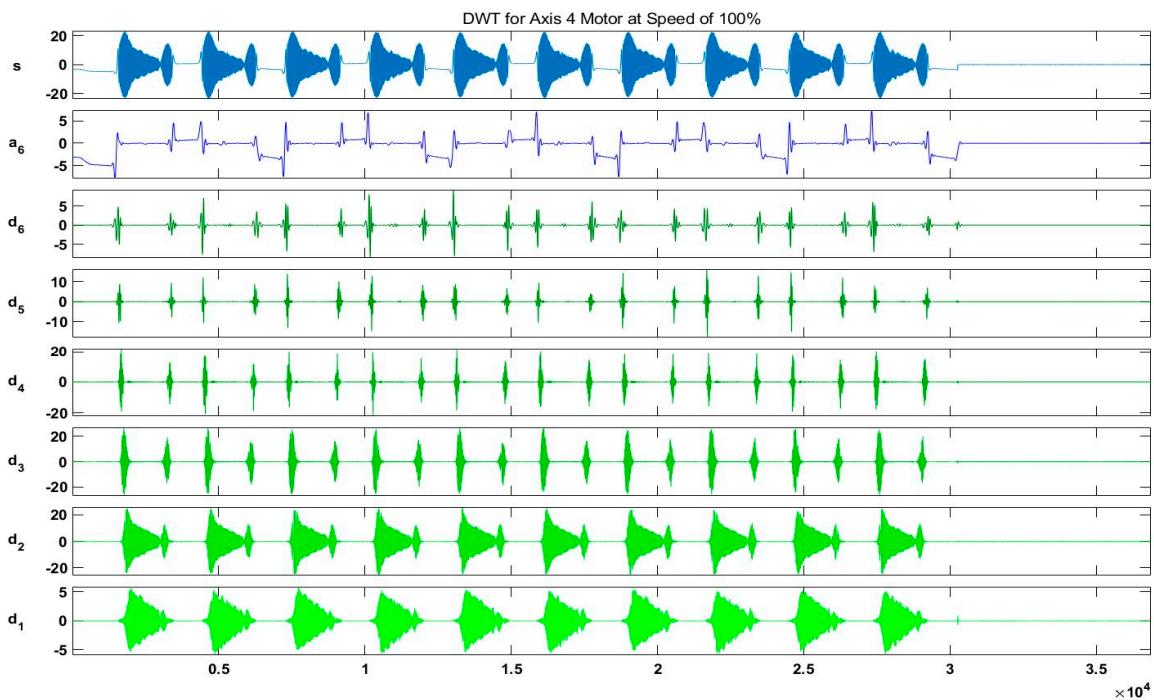


Figure 19. Output results of the DWT for I_q component of the current signal at a speed of 100%.

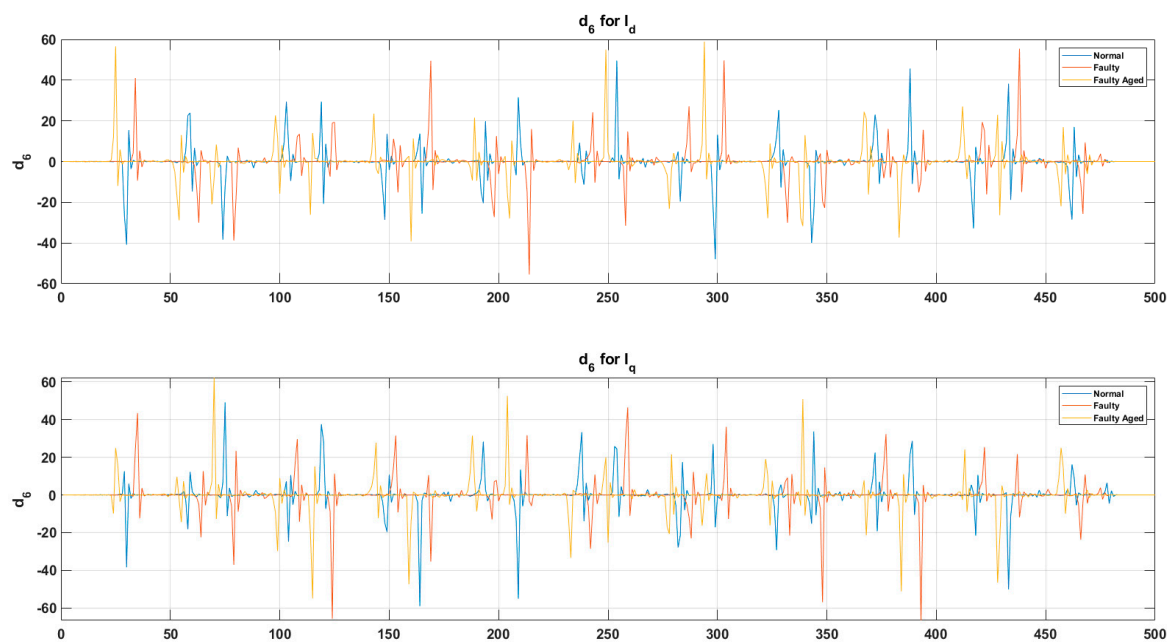


Figure 20. Detailed view of the D6 decomposed wavelet coefficient for each fault scenario.

These decomposed wavelets were utilized for further deterministic analysis. Several features presented in Tables 3 and 4 were extracted from each decomposed wavelet coefficient. Figure 21 shows the response of the wavelet specific features, while Figure 22 shows the response of the wavelet-based statistical features extracted at different speeds of rotation of the motor. The presented results are for the detailed coefficient $D6$. It is apparent that among these features, some features show a very clear difference between the fault categories at some certain speed, though devoid of an overall constant pattern for all of the speed profiles, due to the natural operating phenomenon of the motor. During the operation of the motor, the amount of current flowing through the windings increases or decreases, depending on the rotation speed. This causes analytical uncertainties for classification systems that rely on the MCSA. The classification systems function by autonomously discovering the patterns in data. In the cases of features with less prominent patterns, the accuracy of the systems falls drastically. In particular, in RV reducer fault detection and diagnosis, it is hard to find some prominent patterns among several features. For this, we utilized the feature selection scheme presented in Figure 12 for prominent feature selection, citing some case studies for each type of feature and classification accuracy. We used four main types of ML-based algorithms for classification, namely (1) linear discriminant analysis (LDA), (2) fine tree (FT), (3) naïve Bayes (NB), and (4) support vector machine (SVM). Figure 23 shows the flowchart of the case study for this paper.

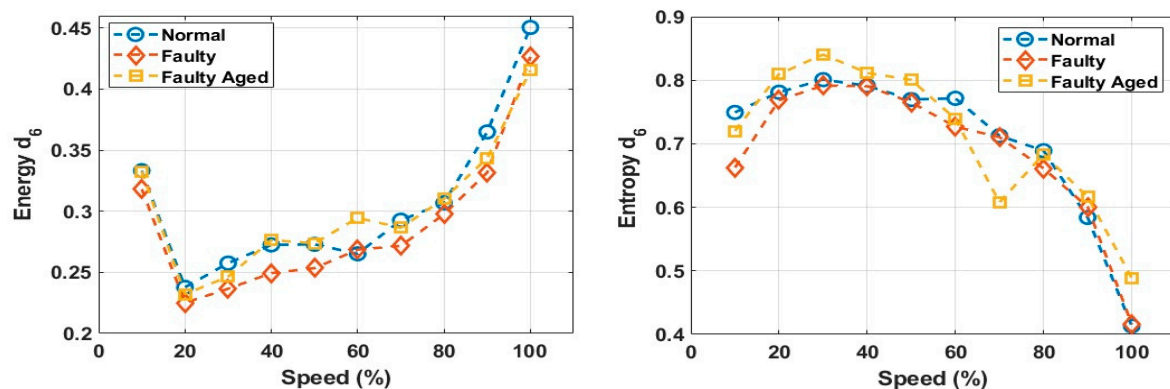


Figure 21. Response of the wavelet specific features at different speeds.

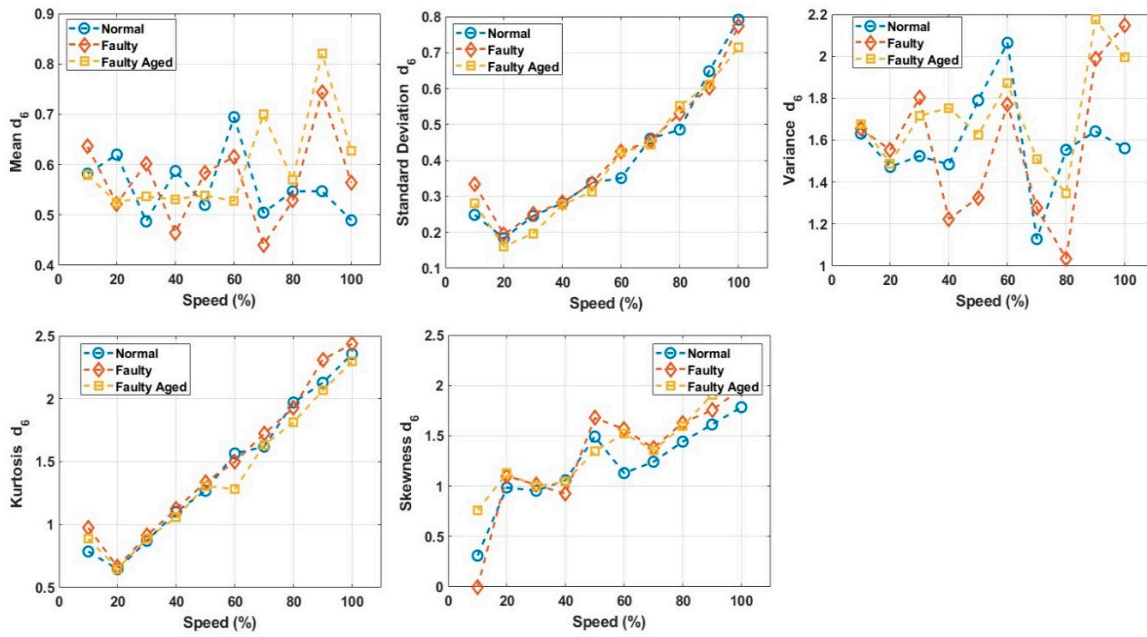


Figure 22. Response of the wavelet-based statistical features at different speeds.

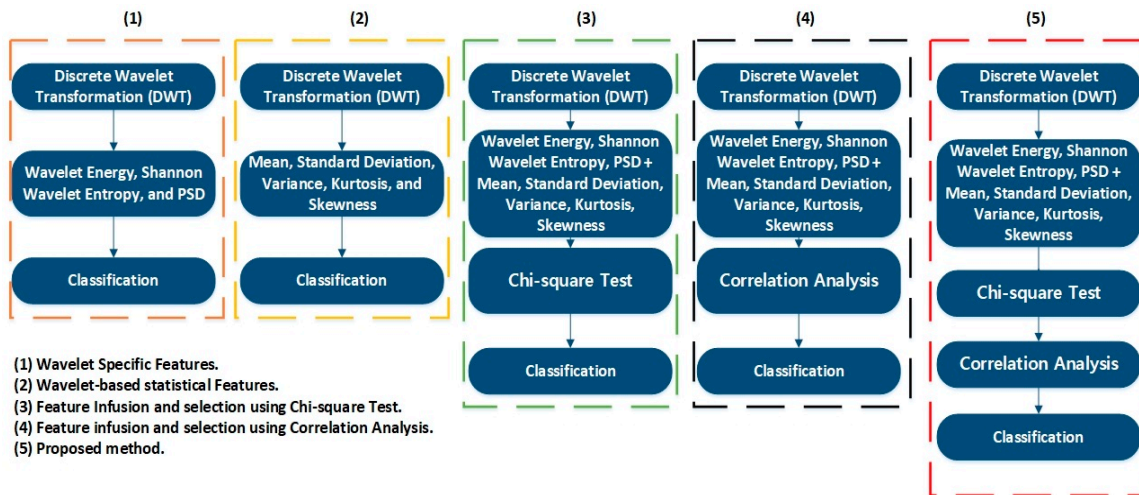


Figure 23. Flowchart of the Case Study.

3.1. Case 1: Wavelet Specific Features

In this case, the 24 wavelet specific features presented in Table 4 were used to train the aforementioned four types of classifiers. We implemented five-fold cross-validation in this work to prevent the model overfitting. The available data were segregated into five disarticulated folds. Among these five folds, four folds were utilized as training samples and one-fold as a testing sample under every training iteration. Every data sample was utilized precisely once as a testing sample. On all folds, the average test error is determined. Using this training and validation scheme, the predictive precision and accuracy of the final model trained with all the data are measured. Figure 24 shows the classification results for the wavelet specific features. The results are presented in the form of a confusion matrix. The rows refer to the predicted output class, whereas columns refer to the true target class. The diagonal cells refer to the classes that are accurately classified. The off-diagonal cells refer to the classes that are inaccurately classified. Each cell presents the number of observations and their percentage. The far-right column in the confusion matrix presents the percentages of all the observations predicted for each class, classified correctly and incorrectly. These matrices are called

the precision and false discovery rate. The overall accuracy of the classifier is given in the cell at the bottom right. The accuracy is calculated using Equation (7):

$$Accuracy = \frac{TP}{TP + FN} \tag{7}$$

where *TP* is true positive and *FN* is false negative. In this case, the maximum accuracy of 73.3% was achieved for the SVM, followed by 66.7%, 50%, and 46.7% for LDA, FT, and NB, respectively.

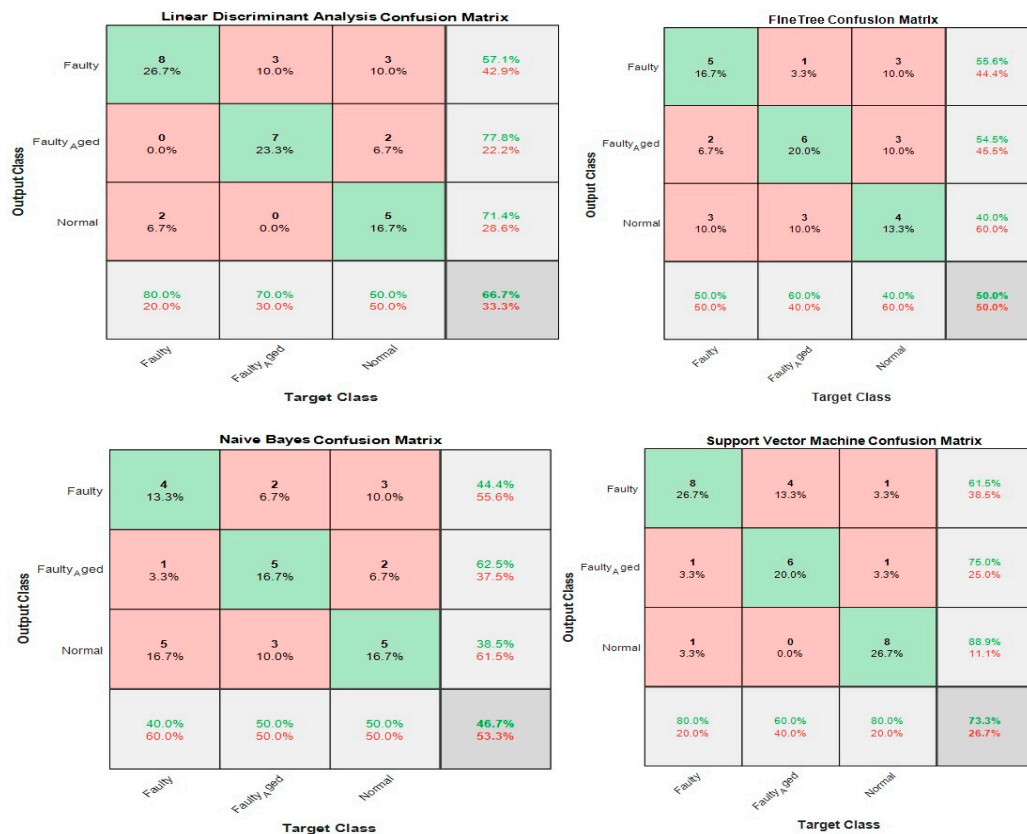


Figure 24. Classification results for Case 1: Wavelet Specific Features.

3.2. Case 2: Wavelet-Based Statistical Features

Table 5 shows the 60 features we used in this case, while Figure 25 shows the classification results for the wavelet-based statistical features. The number of features used is based only on the statistics (Table 5). The maximum accuracy of 50% was achieved for the LDA, followed by (43.3%, 36.7%, and 30.0% for SVM, NB, and FT, respectively). The accuracy achieved was very poor, and this is because the statistical features, such as mean, standard deviation, variance, kurtosis, and skewness, somehow relate to one another in statistical characteristics. While using these kinds of features, there are more chances for the classifier to become confused among several parameters. Regardless of this fact, these features were not ignored and eliminated from performing any kind of classifications; rather, we implemented a feature selection and infusion scheme to distinguish meaningful features, which will be discussed in cases 3, 4, and 5.

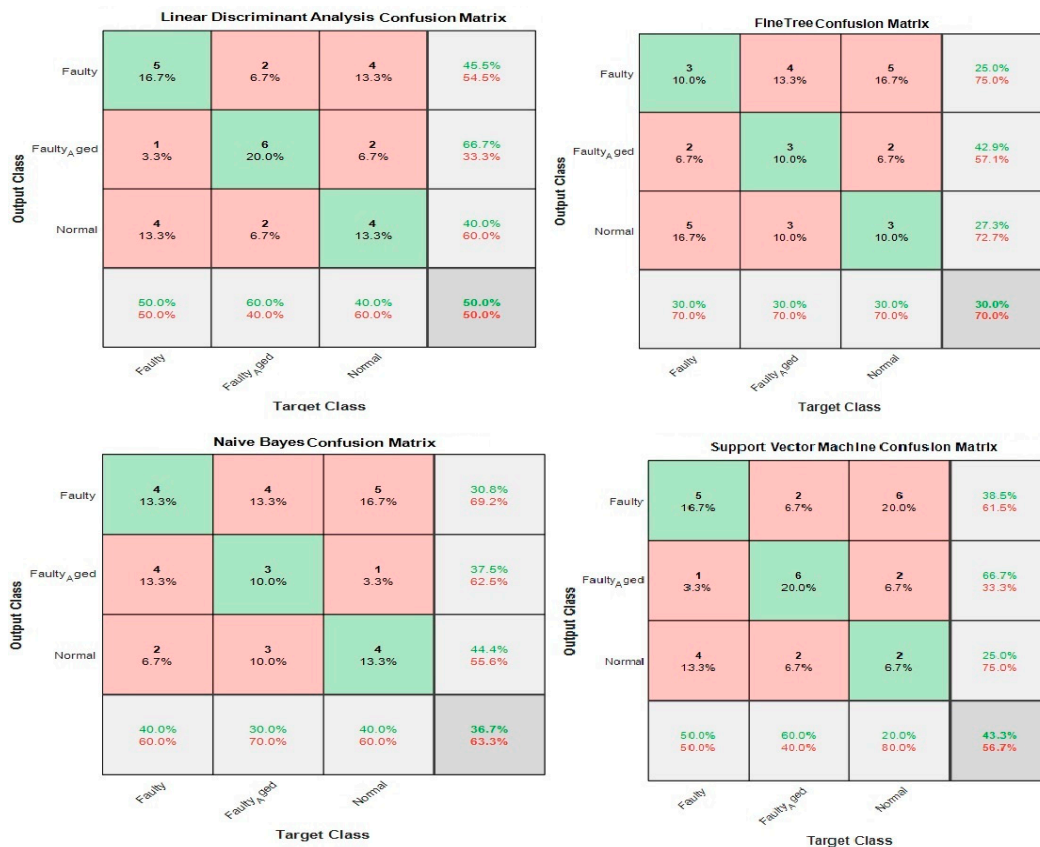


Figure 25. Classification results for Case 2: Wavelet-based Statistical Features.

3.3. Case 3: Feature Infusion and Selection Using Chi-Square Test

In this case, we utilized the typically used statistical features selection algorithm, univariate feature ranking for classification, using chi-square tests *fschi2* for the selection of prominent features among the features presented in Tables 4 and 5. *fschi2* explores if all predictor variables are independent of response variables, by utilizing individual chi-square tests.

The chi-square test of independence decides if there is a relation among categorical variables (i.e., if the variables are independent, or associated). A nonparametric test is commonly used to test the statistical independence or relation among two or more categorical variables. This test uses a contingency table to evaluate the data. A contingency table is a structure in which data are categorized according to two categorical variables. It is also known as a cross-tabulation or a two-way table. For one variable, the categories appear in rows, while for the other variable, they appear in columns. Two or more categories should be used with each variable. Each cell in the table represents the total number of cases for a certain category pair. Equation (8) gives the mathematical representation of the *fschi2*:

$$X^2 = \sum_{i=1}^R \sum_{j=1}^C \frac{(o_{ij} - e_{ij})^2}{e_{ij}} \quad (8)$$

where o_{ij} are the observed cell count in the i th row and j th column of the table, and e_{ij} is the expected cell count in the i th row and j th column of the table. This can be calculated as in Equation (9):

$$e_{ij} = \frac{\text{row } i \text{ total} * \text{col } j \text{ total}}{\text{grand total}} \quad (9)$$

Using the above equations, the number of features was reduced from 84 to 20 (combined features of Tables 4 and 5). The 20 most valuable features with high importance scores were selected,

and classification was performed. Figure 26 shows an example of the categorization of features based on importance. Table 6 gives the details of the 20 most prominent features selected with high importance score. Figure 27 shows the classification results for feature infusion and selection using chi-square test. The maximum accuracy of 73.3% was achieved for the LDA and FT, followed by 70% and 36.7% for SVM and NB, respectively.

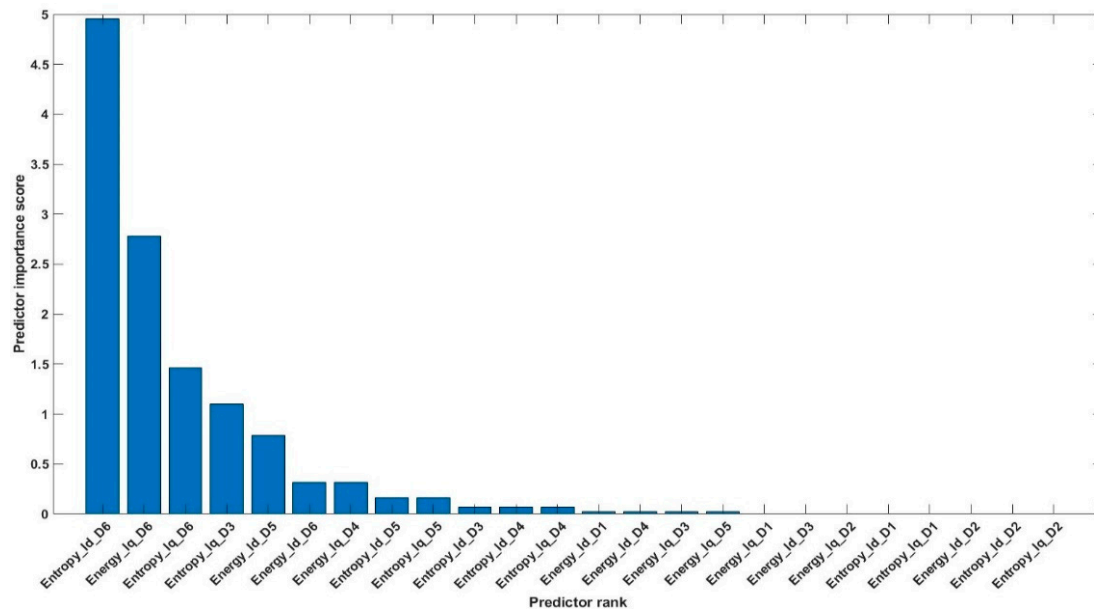


Figure 26. Example of categorization of features based on importance score.

Table 6. Prominent features for Case 2.

No.	Feature
1	SKW_Iq_D6
2	VAR_Id_D6
3	VAR_Iq_D6
4	Mean_Id_D1
5	Mean_Id_D5
6	Mean_Iq_D3
7	STD_Id_D3
8	STD_Iq_D5
9	VAR_Id_D5
10	VAR_Iq_D4
11	Entropy_Id_D6
12	Energy_Iq_D6
13	Entropy_Iq_D6
14	Entropy_Iq_D3
15	Energy_Id_D5
16	Energy_Id_D6
17	Energy_Iq_D4
18	Entropy_Id_D5
19	Energy_Iq_D2
20	Entropy_Id_D1

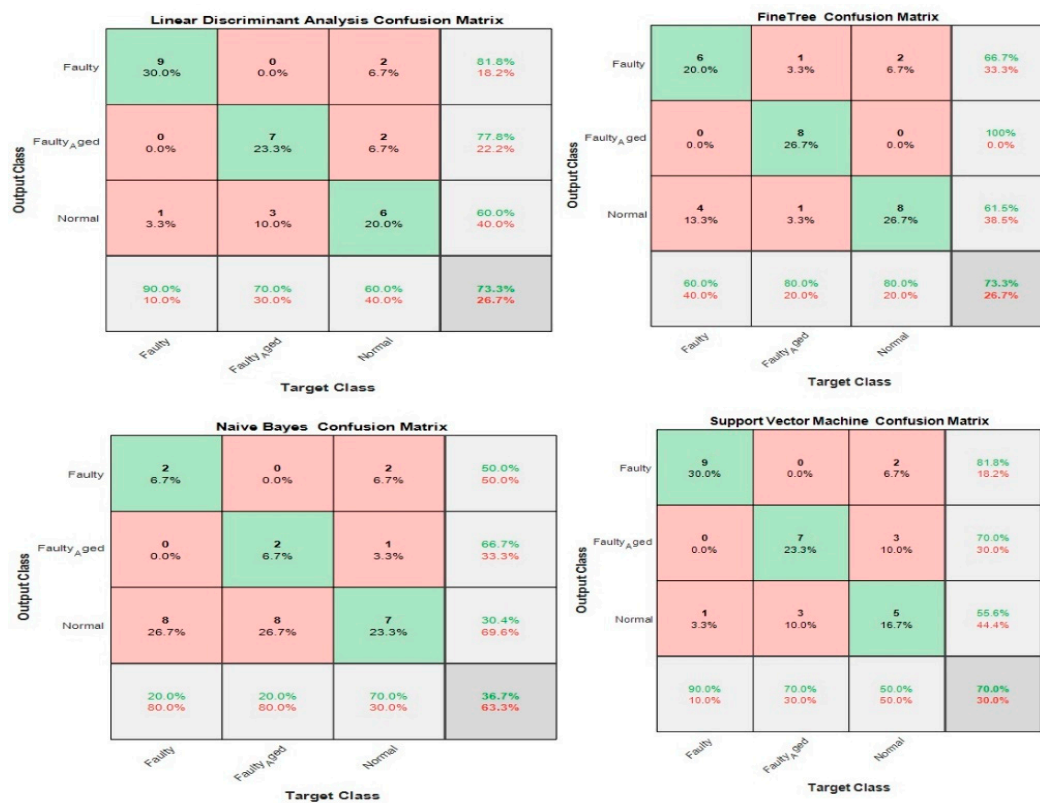


Figure 27. Classification results for Case 3: Feature infusion and selection using Chi-Square Test.

3.4. Case 4: Feature Infusion and Selection Using Correlation Analysis

Only categorical variables can be compared in the chi-square independence test. It cannot equate continuous variables or continuous variables with categorical variables. Moreover, it assesses only the associations between categorical variables, and cannot provide any inferences about causation. This can be observed also by the accuracy results achieved in the previous case (case 3).

In this case, to evaluate the difference in performance between the chi-square test and correlation analysis, we utilized the correlation analysis, rather than chi-square tests, to select the prominent features from both the wavelet specific and wavelet-based statistical features. The correlation analysis is used to determine the correlation between two variables. These variables can be two independent or a dependent and independent variable. We measure the Pearson product moment coefficient of correlation, in particular, as a sample correlation. The sample correlation coefficient is represented by ρ and its values range from -1 to $+1$. There can be a positive or negative correlation between the two variables. The positive correlation means that the variables are highly correlated to each other and vice versa for the negative correlation. The sign of the coefficient of correlation shows the orientation of the relationship. The magnitude of the coefficient of correlation shows the strength of the relationship. Mathematically, it is given in Equation (10):

$$\rho_{xy} = \frac{\sum_{i=1}^n (x_i - \bar{x})(y_i - \bar{y})}{\sqrt{\sum_{i=1}^n (x_i - \bar{x})^2} \sqrt{\sum_{i=1}^n (y_i - \bar{y})^2}} \quad (10)$$

where n is the sample size, x_i , y_i are the individual sample points indexed with i , and $\bar{x} = \frac{1}{n} \sum_{i=1}^n x_i$ is the sample mean. We selected the 20 most prominent features presented in Table 7. These features were carefully selected by analyzing the correlogram. Figure 28 shows an example of one of the correlograms used to select features. The features that had the lowest values for the correlation coefficients were selected. The features with a higher correlation coefficient value of more than 90% mean that these

features show similarities, and can be neglected, to avoid confusion in the training and testing of ML-based classifiers. Figure 29 shows the classification results for feature infusion and selection using chi-square test. The maximum accuracy of 86.7% was achieved for the SVM, followed by 80%, 60%, and 36.7% for LDA, FT, and NB, respectively.

Table 7. Prominent features for Case 4.

No.	Feature
1	Mean_Id_D1
2	Mean_Id_D2
3	STD_Id_D6
4	VAR_Id_D1
5	VAR_Id_D2
6	KRT_Id_D6
7	SKW_Id_D1
8	SKW_Id_D2
9	VAR_Id_D3
10	Mean_Id_D3
11	Energy_Id_D1
12	Energy_Id_D3
13	Energy_Id_D4
14	Energy_Id_D5
15	Energy_Id_D6
16	Energy_Iq_D1
17	Entropy_Id_D3
18	Entropy_Id_D5
19	Entropy_Id_D6
20	Entropy_Iq_D1

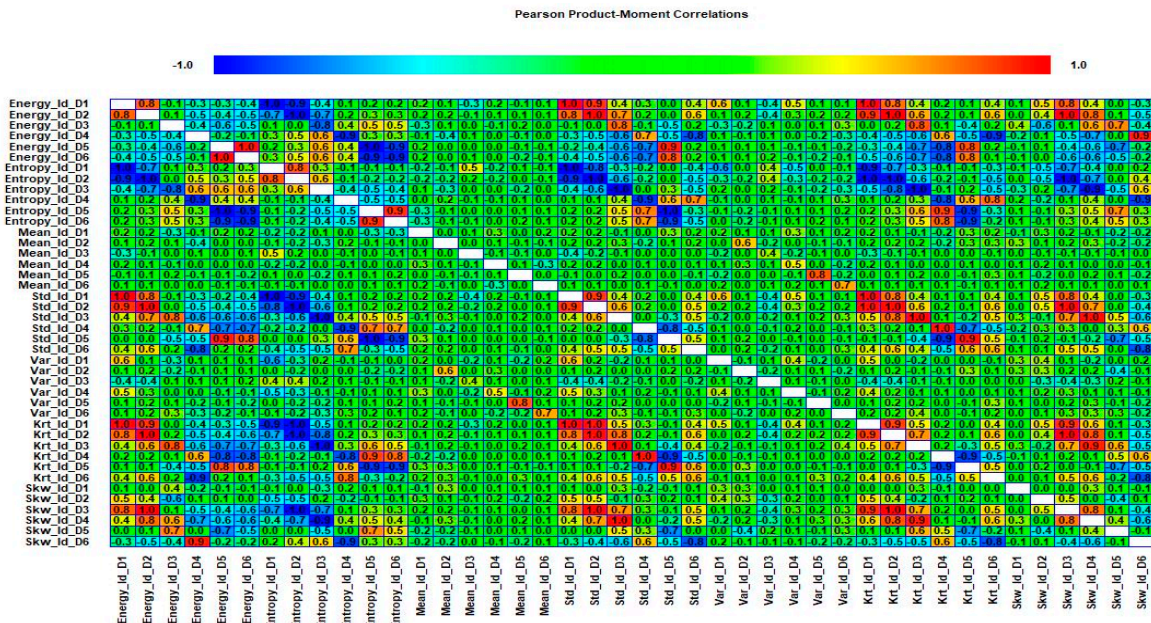


Figure 28. Case 4: An example of one of the correlograms used to select features.

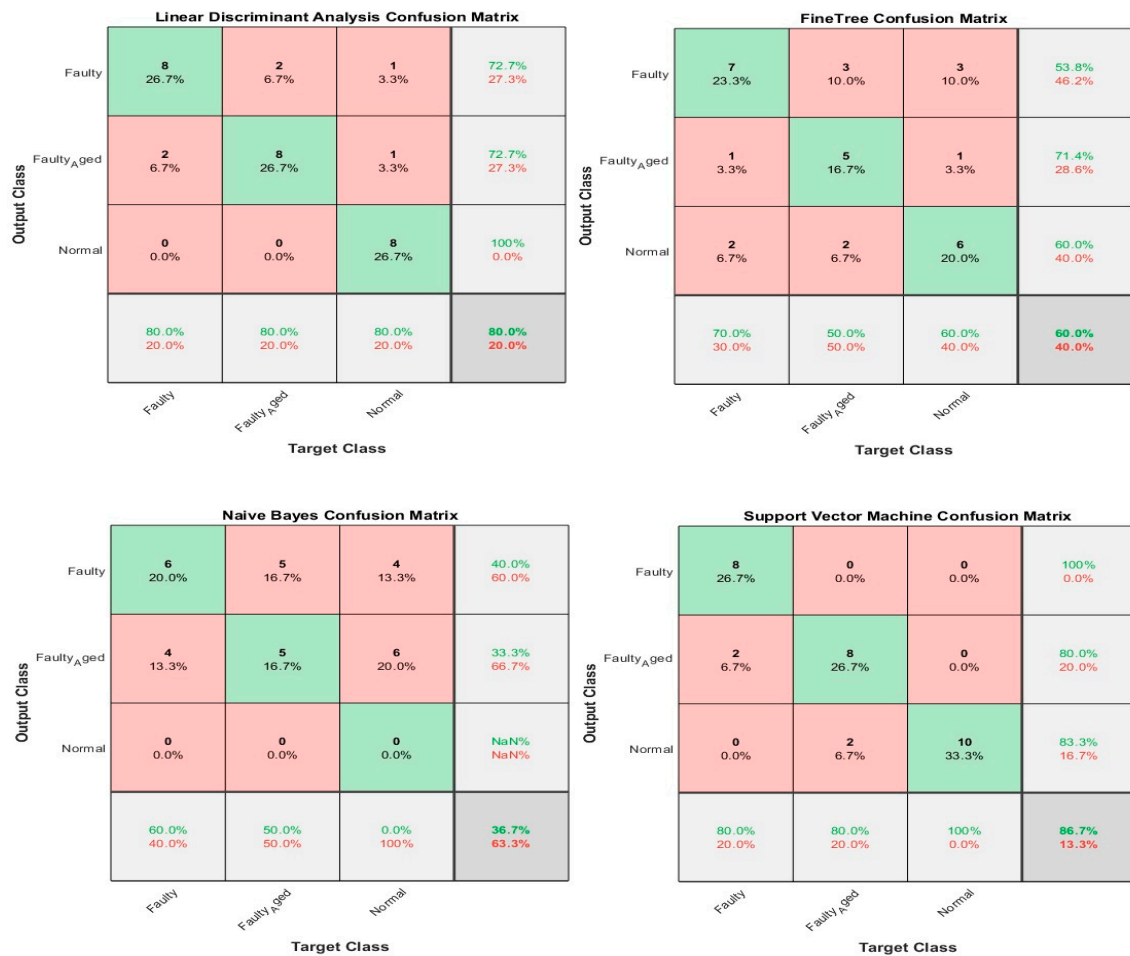


Figure 29. Classification results for Case 4: Feature infusion and selection using Correlation Analysis.

3.5. Case 5: Proposed Feature Infusion Method

The correlation analysis performed well in the process of feature selection then chi-square tests, but the accuracy achieved with a high number of features was still low. Generally, for ML-based classification, the number of features is indirectly proportional to the number of observations (Equation (11)):

$$Number\ of\ Features = \frac{1}{Number\ of\ Observations} \tag{11}$$

The less the number of observations, the more the number of features. In our case, the total number of observations for each class is 10. A lesser number of observations requires more features to achieve higher classification accuracy. On the other hand, a high number of features might also confuse the classifier among several classes, and a good classification accuracy might still not be achieved. Therefore, we combined both chi-square tests and correlation analysis to obtain a balance between the number of features and observations for higher classification accuracy. Figure 23 shows that the proposed method works in two steps of feature selection. First, the chi-square tests were performed to get the importance score of all the features; and among these features, the 20 most prominent features were selected. These selected features were further analyzed, using correlation analysis. Figure 30 shows the correlogram of these features. From these 20 features, we selected the 10 features with a correlation of less than 80%. Table 8 presents these 10 features. Figure 31 shows the classification results for the proposed feature infusion method. The maximum accuracy of 96.7% was achieved for the LDA, followed by 93.3%, 70%, and 33.3% for SVM, FT, and NB, respectively.

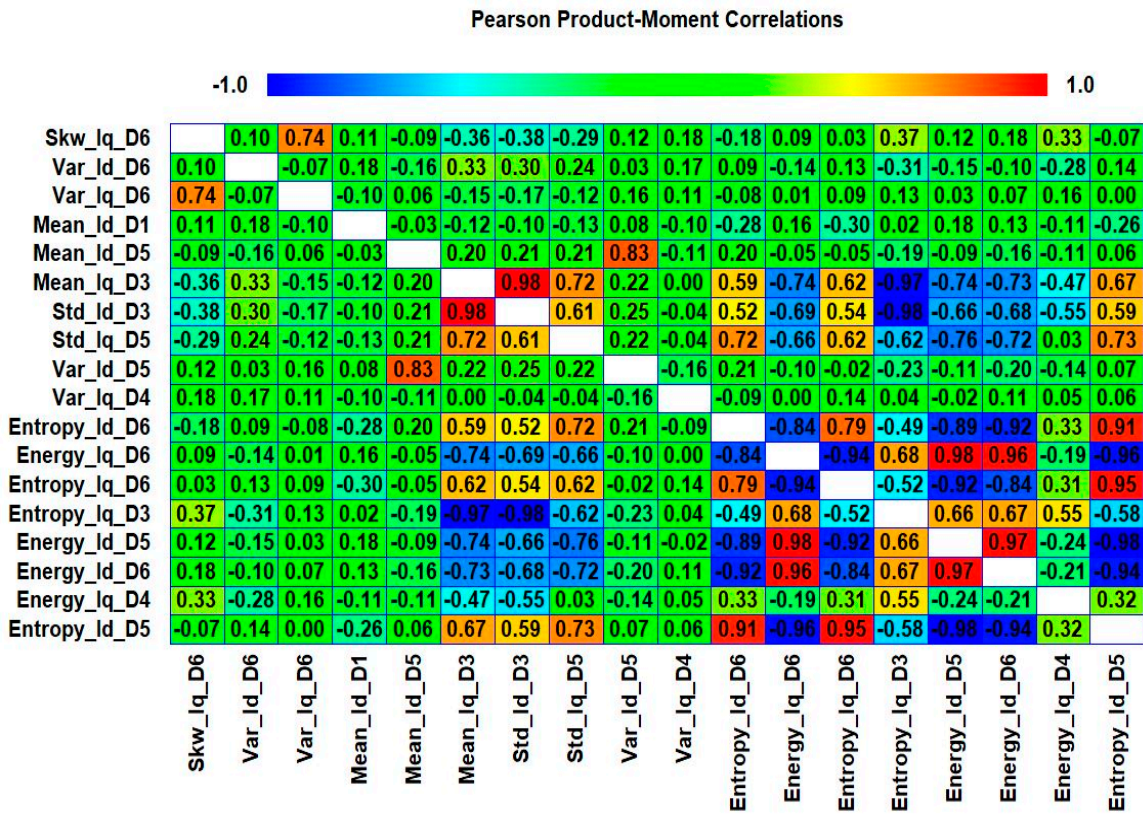


Figure 30. Case 5: The correlogram used to select features.

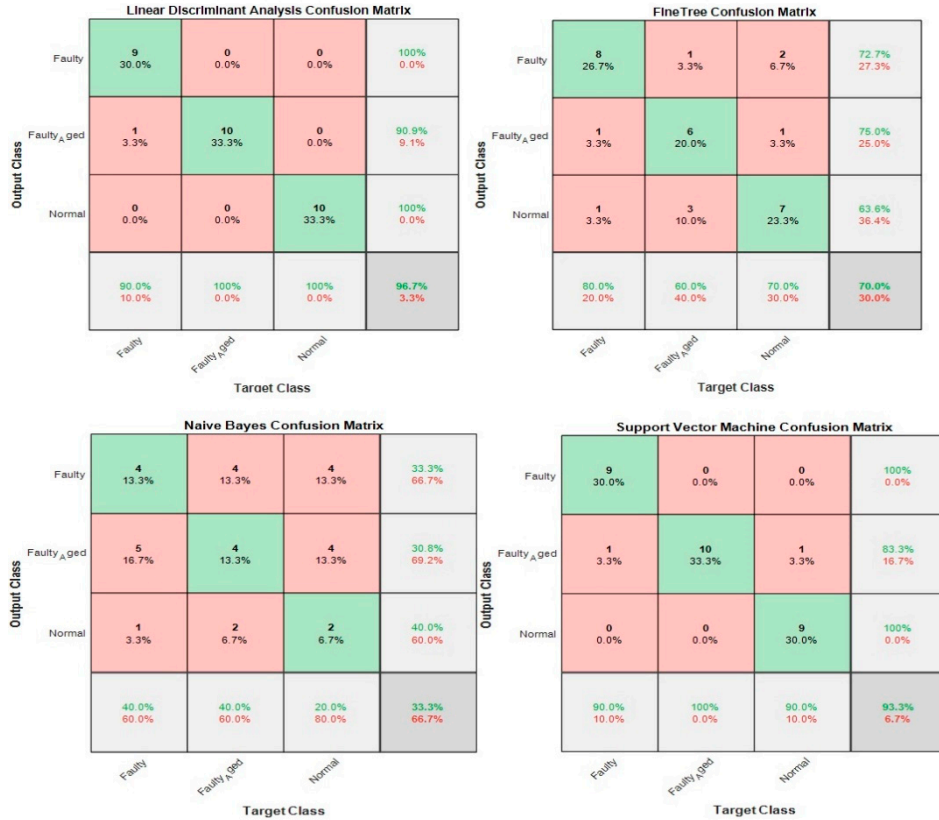


Figure 31. Classification results for Case 5: The Proposed Feature Infusion Method.

Table 8. Selected prominent features for Case 5.

No.	Feature
1	SKW_Iq_D6
2	VAR_Id_D6
3	VAR_Id_D6
4	Mean_Id_D1
5	STD_Iq_D5
6	VAR_Iq_D4
7	Entropy_Id_D6
8	Energy_Iq_D6
9	Entropy_Iq_D6
10	Entropy_Iq_D3

3.6. Comparative Study for Different Cases and Other Methods

Table 9 compares the results among different cases. The results in Table 9 prove that the proposed method works well in detecting and diagnosing the RV reducer fault with high accuracy and a lesser number of features. The average accuracy score calculated (Equation (12)) for the proposed method is 73.3, which is much higher than the score of all the other feature selection and infusion cases. Notice that not all the selected classifiers are suitable for fault diagnosis as different classifiers works based on different algorithms. The choice of classifiers can be made based on the type of problem. In our case, the NB performs poorly in the classification of faults because NB works on an algorithm based on Bayes' theorem. Whereas the LDA shows the best case, and its because LDA is a commonly used multi-variate classification method that aims to find a linear combination of features for class separation which suits perfectly for the type of problem and data we had to deal with in this work. The rightmost side of Table 9 presents the classifier's average performance score (Equation (13)), based on each case. Among the four classifiers, the LDA and SVM performed better than the FT and NB.

Table 9. Performance Comparison.

Classifiers	Case 1	Case 2	Case 3	Case 4	Case 5 (Proposed)	Average Performance Score
LDA	66.7%	50%	73.3%	80%	96.7%	73.34
Fine Tree	50%	30%	73.3%	60%	70%	56.66
Naïve Bayes	46.7%	36.7%	36.7%	36.7%	33.3%	38.02
SVM	73.3%	43.3%	70%	86.7%	93.3%	73.32
Average Accuracy Score	59.175	40	63.325	65.85	73.325	
Number of Features	24	60	20	20	10	

$$\text{Average Accuracy Score} = \frac{\sum_{i=1}^N \text{Accuracy}}{N} \quad (12)$$

$$\text{Classifier Average Performance Score} = \frac{\sum_{j=1}^K \text{Accuracy}}{K} \quad (13)$$

In Equations (12) and (13), N is the total number of classifiers and is given as $N = 1$ (LDA), 2 (FT), 3 (NB), 4 (SVM), while K is the total number of cases, and is given as $K = 1, 2, 3, 4, 5$.

The comparison results among different methods used to detect and diagnose faults are presented in the Table 10. We present a comparison among different techniques and methodologies related to chi-square features [56], discrete wavelet transform with ANN [57], statistically locally linear embedding with SVM [58]. Viney et al. [56], proposed methods where chi-square features were used to classify the faults. Different classifiers with a different number of features were used for this purpose. The accuracy achieved was different for the different number of features. For eight features, the accuracy was 93.33% but for seven features the accuracy reduced to 92%. Just reducing

one feature reduced the accuracy by 1%. Compared to our proposed methodology, we presented a consolidated approach for feature extraction and selection giving us the advantage to reduce the number of features and achieve higher classification accuracy at the same time. On the other hand, Konar et al. [57], used DWT with an artificial neural network (ANN) as a classifier. The accuracy achieved for this method was 93.33%. Also, the use of ANN is computationally heavy as compared to other classifying algorithms such as LDA, SVM, etc. Wang et al. [58], utilized statistical locally linear embedding with SVM as a classifier. The accuracy was recorded as 94.07% which is higher than the other methods. The SVM performed well for the classification of the faults but still, the accuracy is not that good enough. Our proposed methodology utilizes the advantages of signal processing and statistical analysis together to form a consolidated approach for the detection and diagnosis of faults. the accuracy achieved was 96.7% which is considerably high than the other methods. The proposed methodology is suitable for the ML-based classifiers and can help reduce the hard work and labor involved in the feature extraction and selection.

Table 10. Comparison among proposed and other methods.

Methods	Accuracy
8 Chi-Square Features +Random Forest	93.33%
7 Chi Square Features +SVM	92%
Discrete Wavelet Transform + ANN	93.33%
Statistical Locally Linear Embedding +SVM	94.07%
DWT + Chi square + Correlation Analysis +LDA (Proposed)	96.7%

4. Conclusions

In an electromechanical system, generally, two types of faults can occur. These faults are electrical faults and mechanical faults. The electrical faults can be categorized into further three categories: (1) power source faults, (2) inverter/converter faults, and (3) machine faults (electric motors faults). The mechanical faults can be categorized as (1) faults related to electric machines and (2) faults related to coupled mechanical components. In the case of electrical faults and mechanical faults related to electrical machines, electric current signal is used to find the abnormality in the related components. On the other hand, the faults related to coupled mechanical components are detected using vibration, acoustic emission, or ferrography analysis. This leads to segregated and more complex ways for any fault detection and diagnosis system. Therefore, in this work, we focused on the detection of the faults related to coupled mechanical components (which is RV reducer in this case) using the electrical current signals rather than typically used vibration, acoustic, or ferrography analysis schemes. We presented an approach to detect and diagnose mechanical faults mainly related to the rotate vector (RV) reducer for an industrial robot. The proposed approach utilizes the embedded current signals of the electric motor's controller to detect the faults, and it provides advantages over typical fault detection and diagnosis methodologies consisting of vibrational, acoustic emission, and ferrography analysis, by (1) eliminating the need to install costly sensors at several locations, and (2) reducing the amount of data involved in the classification process of the faults. Furthermore, this work introduces a feature infusion scheme that focuses on the time-frequency domain analysis of the recorded current signals using DQ0 and DWT with prominent feature selection for ML-based classification. Real-time analysis was performed on an experimental test bench comprising a Hyundai Robot. The classification accuracy achieved for classifying the faults was 96.7%. The results obtained for the proposed approach show that it works well in classifying the faults for RV reducer. In the future, we are working towards the addition of more mechanical components such as strain wave gear and to find a general approach for the fault detection and diagnosis for an industrial robot using AI.

Author Contributions: Conceptualization, A.R. and H.S.K.; methodology, A.R.; software, A.R. and I.R.; validation, A.R., I.R. and H.S.K.; investigation, A.R.; resources, H.S.K.; data curation, A.R.; writing—original draft preparation, A.R.; writing—review and editing, A.R.; visualization, I.R.; supervision, H.S.K.; project administration, A.R. and H.S.K.; funding acquisition, H.S.K. All authors have read and agreed to the published version of the manuscript.

Funding: This research was financially supported by the Ministry of Trade, Industry, and Energy (MOTIE) and the Korea Institute for Advancement of Technology (KIAT) through the International Cooperative R&D program (Project No. P059500003).

Conflicts of Interest: The authors declare no conflict of interest.

References

- Lee, J.; Wu, F.; Zhao, W.; Ghaffari, M.; Liao, L.; Siegel, D. Prognostics and health management design for rotary machinery systems—Reviews, methodology and applications. *Mech. Syst. Signal Process.* **2014**, *42*, 314–334. [[CrossRef](#)]
- Lall, P.; Hande, M.; Bhat, C.; Suhling, J.; Islam, N. *Prognostics and Health Management of Electronics*; Wiley: Hoboken, NJ, USA, 2009.
- Carvalho Bittencourt, A. *Modeling and Diagnosis of Friction and Wear in Industrial Robots*; Linköping Studies in Science and Technology. Dissertations; Linköping University Electronic Press: Linköping, Sweden, 2014; Volume 1617, ISBN 9789175192512.
- Abichou, B.; Voisin, A.; Jung, B. Bottom-up capacities inference for health indicator fusion within multi-level industrial systems. In Proceedings of the 2012 IEEE Conference on Prognostics and Health Management, Denver, CO, USA, 18–21 June 2012; IEEE: Denver, CO, USA, 2012; pp. 1–7.
- Sheppard, J.W.; Kaufman, M.A.; Wilmering, T.J. IEEE Standards for Prognostics and Health Management. In Proceedings of the 2008 IEEE AUTOTESTCON, Salt Lake City, UT, USA, 8–11 September 2008.
- Yang, J.; Kim, J. An accident diagnosis algorithm using long short-term memory. *Nucl. Eng. Technol.* **2018**, *50*, 582–588. [[CrossRef](#)]
- Zhang, L.; Lin, J.; Karim, R. Adaptive kernel density-based anomaly detection for nonlinear systems. *Knowl. Based Syst.* **2018**, *139*, 50–63. [[CrossRef](#)]
- Fan, J.; Yung, K.C.; Pecht, M. Physics-of-Failure-Based Prognostics and Health Management for High-Power White Light-Emitting Diode Lighting. *IEEE Trans. Device Mater. Reliab.* **2011**, *11*, 407–416. [[CrossRef](#)]
- Pecht, M.; Jie, G. Physics-of-failure-based prognostics for electronic products. *Trans. Inst. Meas. Control* **2009**, *31*, 309–322. [[CrossRef](#)]
- Tsui, K.L.; Chen, N.; Zhou, Q.; Hai, Y.; Wang, W. Prognostics and Health Management: A Review on Data Driven Approaches. *Math. Probl. Eng.* **2015**, *2015*, 1–17. [[CrossRef](#)]
- Gao, Z.; Cecati, C.; Ding, S. A Survey of Fault Diagnosis and Fault-Tolerant Techniques Part II: Fault Diagnosis with Knowledge-Based and Hybrid/Active Approaches. *IEEE Trans. Ind. Electron.* **2015**, 1–1. [[CrossRef](#)]
- Huang, G.-B.; Wang, D.H.; Lan, Y. Extreme learning machines: A survey. *Int. J. Mach. Learn. Cybern.* **2011**, *2*, 107–122. [[CrossRef](#)]
- LeCun, Y.; Bengio, Y.; Hinton, G. Deep learning. *Nature* **2015**, *521*, 436–444. [[CrossRef](#)] [[PubMed](#)]
- Xu, Y.; Sun, Y.; Wan, J.; Liu, X.; Song, Z. Industrial Big Data for Fault Diagnosis: Taxonomy, Review, and Applications. *IEEE Access* **2017**, *5*, 17368–17380. [[CrossRef](#)]
- Liao, L.; Kottig, F. Review of Hybrid Prognostics Approaches for Remaining Useful Life Prediction of Engineered Systems, and an Application to Battery Life Prediction. *IEEE Trans. Reliab.* **2014**, *63*, 191–207. [[CrossRef](#)]
- Cerrada, M.; Sánchez, R.-V.; Li, C.; Pacheco, F.; Cabrera, D.; Valente de Oliveira, J.; Vásquez, R.E. A review on data-driven fault severity assessment in rolling bearings. *Mech. Syst. Signal Process.* **2018**, *99*, 169–196. [[CrossRef](#)]
- Wang, D.; Tsui, K.-L.; Miao, Q. Prognostics and Health Management: A Review of Vibration Based Bearing and Gear Health Indicators. *IEEE Access* **2018**, *6*, 665–676. [[CrossRef](#)]
- Lall, P.; Lowe, R.; Goebel, K. Prognostics and health monitoring of electronic systems. In Proceedings of the 2011 12th Intl. Conf. on Thermal, Mechanical & Multi-Physics Simulation and Experiments in Microelectronics and Microsystems, Linz, Austria, 18–20 April 2011; pp. 1–17.
- Thompson, N.C.; Greenewald, K.; Lee, K.; Manso, G.F. The Computational Limits of Deep Learning. *arXiv* **2020**, arXiv:2007.05558.

20. Marsland, S. Machine Learning. In *Machine Learning*; CRC Press, Taylor & Francis Inc.: Boca Raton, FL, USA, 2014.
21. Silver, D.; Huang, A.; Maddison, C.J.; Guez, A.; Sifre, L.; Van den Driessche, G.; Schrittwieser, J.; Antonoglou, I.; Panneershelvam, V.; Lanctot, M.; et al. Mastering the game of Go with deep neural networks and tree search. *Nature* **2016**, *529*, 484–489. [[CrossRef](#)] [[PubMed](#)]
22. Bojarski, M.; Del Testa, D.; Dworakowski, D.; Firner, B.; Flepp, B.; Goyal, P.; Jackel, L.D.; Monfort, M.; Muller, U.; Zhang, J.; et al. End to End Learning for Self-Driving Cars. *arXiv* **2016**, arXiv:1604.07316.
23. He, K.; Zhang, X.; Ren, S.; Sun, J. Delving deep into rectifiers: Surpassing human-level performance on imagenet classification. In Proceedings of the IEEE International Conference on Computer Vision, Santiago, Chile, 7–13 December 2015; IEEE: Piscataway, NJ, USA, 2015; pp. 1026–1034.
24. Liu, S.; Tian, Y. Facial Expression Recognition Method Based on Gabor Wavelet Features and Fractional Power Polynomial Kernel PCA. In *Advances in Neural Networks-ISNN 2010*; Zhang, L., Lu, B.-L., Kwok, J., Eds.; Lecture Notes in Computer Science; Springer: Berlin/Heidelberg, Germany, 2010; Volume 6064, pp. 144–151, ISBN 9783642133176.
25. Waibel, A.; Lee, K.-F. *Readings in Speech Recognition*; Elsevier: Amsterdam, The Netherlands, 1990; ISBN 0080515843.
26. Pazzani, M.; Billsus, D. Learning and revising user profiles: The identification of interesting web sites. *Mach. Learn.* **1997**, *27*, 313–331. [[CrossRef](#)]
27. Chan, P.K.; Stolfo, S.J. Learning with Non-Uniform Class and Cost Distributions: Effects and a Distributed Multi-Classifer Approach. In Workshop Notes KDD-98 Workshop on Distributed Data Mining. 1998, pp. 1–9. Available online: <http://citeseerx.ist.psu.edu/viewdoc/summary?doi=10.1.1.35.3392> (accessed on 27 November 2020).
28. Guzella, T.S.; Caminhas, W.M. A review of machine learning approaches to spam filtering. *Expert Syst. Appl.* **2009**, *36*, 10206–10222. [[CrossRef](#)]
29. Huang, C.-L.; Chen, M.-C.; Wang, C.-J. Credit scoring with a data mining approach based on support vector machines. *Expert Syst. Appl.* **2007**, *33*, 847–856. [[CrossRef](#)]
30. Randall, R.B.; Antoni, J. Rolling element bearing diagnostics—A tutorial. *Mech. Syst. Signal Process.* **2011**, *25*, 485–520. [[CrossRef](#)]
31. Sinha, J.K.; Elbhah, K. A future possibility of vibration based condition monitoring of rotating machines. *Mech. Syst. Signal Process.* **2013**, *34*, 231–240. [[CrossRef](#)]
32. Siegel, D.; Ly, C.; Lee, J. Methodology and framework for predicting helicopter rolling element bearing failure. *IEEE Trans. Reliab.* **2012**, *61*, 846–857. [[CrossRef](#)]
33. Zhen, L.; Zhengjia, H.; Yanyang, Z.; Xuefeng, C. Bearing condition monitoring based on shock pulse method and improved redundant lifting scheme. *Math. Comput. Simul.* **2008**, *79*, 318–338. [[CrossRef](#)]
34. Cabal-Yepez, E.; Garcia-Ramirez, A.G.; Romero-Troncoso, R.J.; Garcia-Perez, A.; Osornio-Rios, R.A. Reconfigurable monitoring system for time-frequency analysis on industrial equipment through STFT and DWT. *IEEE Trans. Ind. Inform.* **2012**, *9*, 760–771. [[CrossRef](#)]
35. Lau, E.C.; Ngan, H.W. Detection of motor bearing outer raceway defect by wavelet packet transformed motor current signature analysis. *IEEE Trans. Instrum. Meas.* **2010**, *59*, 2683–2690. [[CrossRef](#)]
36. Delgado, M.; Cirrincione, G.; Garcia, A.; Ortega, J.A.; Henao, H. A novel condition monitoring scheme for bearing faults based on curvilinear component analysis and hierarchical neural networks. In Proceedings of the 2012 XXth International Conference on Electrical Machines, Marseille, France, 2–5 September 2012; pp. 2472–2478.
37. Jin, X.; Zhao, M.; Chow, T.W.; Pecht, M. Motor bearing fault diagnosis using trace ratio linear discriminant analysis. *IEEE Trans. Ind. Electron.* **2013**, *61*, 2441–2451. [[CrossRef](#)]
38. Zhou, W.; Lu, B.; Habetler, T.G.; Harley, R.G. Incipient bearing fault detection via motor stator current noise cancellation using wiener filter. *IEEE Trans. Ind. Appl.* **2009**, *45*, 1309–1317. [[CrossRef](#)]
39. Thollon, F.; Grellet, G.; Jammal, A. Asynchronous motor cage fault detection through electromagnetic torque measurement. *Eur. Trans. Electr. Power* **1993**, *3*, 375–378. [[CrossRef](#)]
40. Elasha, F.; Greaves, M.; Mba, D.; Addali, A. Application of acoustic emission in diagnostic of bearing faults within a helicopter gearbox. *Procedia Cirp* **2015**, *38*, 30–36. [[CrossRef](#)]
41. Beguenane, R.; Benbouzid, M.E.H. Induction motors thermal monitoring by means of rotor resistance identification. *IEEE Trans. Energy Convers.* **1999**, *14*, 566–570. [[CrossRef](#)]

42. Nejari, H.; Benbouzid, M.E.H. Monitoring and diagnosis of induction motors electrical faults using a current Park's vector pattern learning approach. *IEEE Trans. Ind. Appl.* **2000**, *36*, 730–735. [[CrossRef](#)]
43. Ondel, O.; Boutleux, E.; Blanco, E.; Clerc, G. Coupling pattern recognition with state estimation using Kalman filter for fault diagnosis. *IEEE Trans. Ind. Electron.* **2011**, *59*, 4293–4300. [[CrossRef](#)]
44. Lei, Y.; Zuo, M.J. Gear crack level identification based on weighted K nearest neighbor classification algorithm. *Mech. Syst. Signal Process.* **2009**, *23*, 1535–1547. [[CrossRef](#)]
45. Bechhoefer, E.; Kingsley, M. A Review of Time Synchronous Average Algorithms. *Annu. Conf. Progn. Health Manag. Soc.* **2009**, *23*, 11.
46. Braun, S. The synchronous (time domain) average revisited. *Mech. Syst. Signal Process.* **2011**, *25*, 1087–1102. [[CrossRef](#)]
47. He, Q.; Liu, Y.; Long, Q.; Wang, J. Time-Frequency Manifold as a Signature for Machine Health Diagnosis. *IEEE Trans. Instrum. Meas.* **2012**, *61*, 1218–1230. [[CrossRef](#)]
48. Portnoff, M. Time-frequency representation of digital signals and systems based on short-time Fourier analysis. *IEEE Trans. Acoust. Speech Signal Process.* **1980**, *28*, 55–69. [[CrossRef](#)]
49. Tarasiuk, T. Hybrid Wavelet-Fourier Spectrum Analysis. *IEEE Trans. Power Deliv.* **2004**, *19*, 957–964. [[CrossRef](#)]
50. Anatonio-Daviu, J.A.; Riera-Guasp, M.; Floch, J.R.; Palomares, M.P.M. *Validation of a New Method for the Diagnosis of Rotor Bar Failures via Wavelet Transform in Industrial Induction Machines*; IEEE: Piscataway, NJ, USA, 2006; Volume 42.
51. Akansu, A.N.; Medley, M.J. (Eds.) *Wavelet, Subband and Block Transforms in Communications and Multimedia*; The International Series in Engineering and Computer Science; Kluwer Academic Publishers: Boston, MA, USA, 2002; Volume 504, ISBN 9780792385073.
52. De Courville, M.; Xueming, L.; Duhamel, P.; Akansu, A.N. Orthogonal transmultiplexers in communication: A review. *IEEE Trans. Signal Process.* **1998**, *46*, 979–995. [[CrossRef](#)]
53. Rohan, A.; Kim, S.H. Fault Detection and Diagnosis System for a Three-Phase Inverter Using a DWT-Based Artificial Neural Network. *Int. J. Fuzzy Log. Intell. Syst.* **2016**, *16*, 238–245. [[CrossRef](#)]
54. Rohan, A.; Kim, S.H. RLC Fault Detection Based on Image Processing and Artificial Neural Network. *Int. J. Fuzzy Log. Intell. Syst.* **2019**, *19*, 78–87. [[CrossRef](#)]
55. Rohan, A.; Rabah, M.; Kim, S.H. An Integrated Fault Detection and Identification System for Permanent Magnet Synchronous Motor in Electric Vehicles. *Int. J. Fuzzy Log. Intell. Syst.* **2018**, *18*, 20–28. [[CrossRef](#)]
56. Vinay, V.; Kumar, G.V.; Kumar, K.P. Application of chi square feature ranking technique and random forest classifier for fault classification of bearing faults. In Proceedings of the 22th International Congress on Sound and Vibration, Florence, Italy, 12–16 July 2015.
57. Konar, P.; Chattopadhyay, P. Bearing fault detection of induction motor using wavelet and support vector machines (SVMs). *Appl. Soft Comput.* **2011**, *11*, 4203–4211. [[CrossRef](#)]
58. Wang, X.; Zheng, Y.; Zhao, Z.; Wang, J. Bearing fault diagnosis based on statistical locally, linear embedding. *Sensors* **2015**, *15*, 16225–16247. [[CrossRef](#)] [[PubMed](#)]

Publisher's Note: MDPI stays neutral with regard to jurisdictional claims in published maps and institutional affiliations.



© 2020 by the authors. Licensee MDPI, Basel, Switzerland. This article is an open access article distributed under the terms and conditions of the Creative Commons Attribution (CC BY) license (<http://creativecommons.org/licenses/by/4.0/>).